

A multi-resolution approach to global ocean modeling



Todd Ringler ^{a,*}, Mark Petersen ^b, Robert L. Higdon ^c, Doug Jacobsen ^a, Philip W. Jones ^a, Mathew Maltrud ^a

^a Theoretical Division, Los Alamos National Laboratory, Los Alamos, NM 87545, USA

^b Computer and Computational Science, Los Alamos National Laboratory, Los Alamos, NM 87545, USA

^c Department of Mathematics, Oregon State University, Corvallis, OR 97331-4605, USA

ARTICLE INFO

Article history:

Received 28 September 2012

Received in revised form 17 April 2013

Accepted 27 April 2013

Available online 11 May 2013

Keywords:

MPAS-Ocean

Global ocean model

Finite-volume

Multi-resolution

Spherical Centroidal Voronoi Tesselations

ABSTRACT

A new global ocean model (MPAS-Ocean) capable of using enhanced resolution in selected regions of the ocean domain is described and evaluated. Three simulations using different grids are presented. The first grid is a uniform high-resolution (15 km) mesh; the second grid has similarly high resolution (15 km) in the North Atlantic (NA), but coarse resolution elsewhere; the third grid is a variable resolution grid like the second but with higher resolution (7.5 km) in the NA. Simulation results are compared to observed sea-surface height (SSH), SSH variance and selected current transports. In general, the simulations produce subtropical and subpolar gyres with peak SSH amplitudes too strong by between 0.25 and 0.40 m. The mesoscale eddy activity within the NA is, in general, well simulated in both structure and amplitude. The uniform high-resolution simulation produces reasonable representations of mesoscale activity throughout the global ocean. Simulations using the second variable-resolution grid are essentially identical to the uniform case within the NA region. The third case with higher NA resolution produces a simulation that agrees somewhat better in the NA with observed SSH, SSH variance and transports than the two 15 km simulations. The actual throughput, including I/O, for the $x1\text{-}15$ km simulation is the same as the structured grid Parallel Ocean Program ocean model in its standard high-resolution 0.1° configuration. Our overall conclusion is that this ocean model is a viable candidate for multi-resolution simulations of the global ocean system on climate-change time scales.

© 2013 Elsevier Ltd. All rights reserved.

1. Introduction

Over the relatively short history of global ocean modeling, the approach has been almost entirely based in structured meshes, conforming quadrilaterals and a desire to obtain quasi-uniform resolution. The first models were situated on a latitude-longitude grid (Bryan, 1969; Cox, 1970; Semtner, 1974) but the grid singularities at the two “grid poles” proved to be problematic. Generalizing the latitude-longitude grid to be a curvilinear grid (Murray and Reason, 2001; Smith et al., 1995) allowed placement of grid poles over land, thus eliminating these singularities from the ocean domain. Since resolution in all regions of these structured, conforming quadrilateral meshes must change in lockstep, doubling resolution requires an additional factor of 10 in computational resources. The ubiquity of this approach is confirmed through the following: all 23 global ocean models used in the Intergovernmental Panel on Climate Change (IPCC) 4th Assessment Report were based on structured, conforming quadrilateral meshes (see Chapter 8, pg 597 of Randall and Bony, 2007).

Our view is that the global ocean modeling community benefits from having a diversity of numerical approaches. While this diversification is well underway with respect to the modeling of the vertical coordinate (Hallberg, 1997; Bleck, 2002), progress in developing new methods for modeling the horizontal structure of the global ocean on climate-change time scales has lagged behind. New multi-resolution approaches, both structured and unstructured, are emerging with applications focused on regional and coastal ocean modeling (Chen et al., 2003; Danilov et al., 2004; Shchepetkin and McWilliams, 2005; White et al., 2008). The challenges in transitioning from coastal and regional applications to global ocean climate applications is clearly discussed in Griffies et al. (2009). These challenges include the following: lack of robust horizontal discretization, lack of high-order advection algorithms, lack of scale-adaptive (aka scale-aware) physical parameterizations, difficulty in analyzing simulations, and computational expense. We place these challenges into two broad categories: formulation of dynamical core and formulation of scale-adaptive physical parameterizations. The formulation of the dynamical core includes issues related to spatial discretization, temporal discretization, transport and computational expense.

The driving requirements for a dynamical core to be applied in coastal applications can be very different from the requirements for a dynamical core to be used for global ocean climate-change

* Corresponding author. Tel.: +1 505 667 7744.

E-mail address: ringler@lanl.gov (T. Ringler).

applications. While issues related to geostrophic adjustment, tracer conservation, vorticity dynamics and computational efficiency have to be considered early in the formulation of a global ocean dynamical core, these same issues can sometimes be significantly less important for models focused toward coastal applications. As a result, there is tension regarding how to construct an ocean dynamical core capable of bridging spatial scales from coastal to global in a single simulation. Should we start with a coastal model and build “up” or start with a global ocean model and build “down”? We do not think that an answer to this question is known at this time, but our decided preference is to build “down”. Essentially, our approach is to construct an ocean dynamical core that, first and foremost, is a viable global ocean model then endow that model with the ability to regionally enhance the grid-scale resolution without degrading the quality of the global simulation.

The model presented below is called MPAS-Ocean. The acronym MPAS represents Model for Prediction Across Scales. MPAS is a set of shared software utilities jointly developed by National Center for Atmospheric Research and Los Alamos National Laboratory for the rapid prototyping of dynamical cores built “on top of” the horizontal discretization developed in Thuburn et al. (2009) and Ringler et al. (2010), along with the variable-resolution Spherical Centroidal Voronoi Tessellations (SCVTs) discussed in Ju et al. (2010). To date, four dynamical cores have been constructed using this framework: a shallow-water model (Ringler et al., 2011), a hydrostatic atmosphere model (Rauscher et al., 2013), a non-hydrostatic atmosphere model (Skamarock et al., 2012), and the ocean model discussed below. A land-ice model similar to Perego et al. (2012) is currently being developed within the MPAS framework. The challenges in creating global, multi-resolution models of the ocean or atmosphere are in many ways similar to those found for coastal models trying to scale up to global domains. Namely, we are challenged to create high-order transport schemes, implement multi-scale time stepping algorithms, develop scale-adaptive physical parameterizations and produce new techniques for analyzing simulations.

A global ocean model capable of resolving multiple resolutions within a single simulation must possess the following three properties before such a model will find widespread use in the ocean modeling community. First, as stated above, the ocean model must be competitive with structured-grid global ocean models with respect to physical correctness and simulation quality. Second, the multi-resolution model must be competitive with existing global ocean models with respect to computational cost per degree of freedom. And finally, the dynamics of a multi-resolution ocean simulation as a function of grid-scale must compare favorably to the suite of global uniform simulations that span these same scales. In other words, simulated ocean dynamics should be insensitive to whether that scale is present in a multi-resolution simulation or a quasi-uniform simulation. A global multi-resolution ocean model that possesses these three properties would provide a compelling alternative to existing structured global ocean models. No such compelling alternative exists at present. Furthermore, the results we present below does not warrant us to definitely conclude that MPAS-O possesses any of these properties, but rather the results strongly suggests such properties are obtainable within the MPAS-O approach.

The construction of a new global ocean climate model is a decade-long endeavor. As such, our goal here is not to present a model that is ready for IPCC-class simulations. Our primary goal is to introduce this modeling approach and provide results responsive to the three properties we discuss immediately above. First, we introduce the MPAS approach by summarizing the properties of the conforming mesh and finite-volume method. Second, we provide evidence that the numerical approach has merit as a global, quasi-uniform ocean model through analysis of the current

structure and mesoscale eddy characteristics. Third, we show that the mesoscale eddy characteristics and mean-flow conditions of the North Atlantic can be reproduced with a variable resolution ocean model that has high resolution only in the North Atlantic region. And finally, we compare the computational performance of MPAS-O to the LANL Parallel Ocean Program (POP). While a plausible representation of the North Atlantic, obtained with acceptable computational expense, is necessary for the acceptance of a new modeling approach, we realize that such results are far from sufficient. Yet, it seems like a reasonable place to begin. This contribution is entirely focused on the evaluation of the dynamical core and omits almost entirely any discussion of scale-adaptive physical parameterizations. This choice simply reflects the reality that global ocean models are built starting from a dynamical core.

A summary of the simulations discussed in Section 5 provides a sense for our motivation and intended scope. The first simulation, $x1\text{-}15\text{ km}$, uses a global quasi-uniform ($x1$) grid with a nominal resolution of 15 km. The second simulation, $x5\text{-}NA\text{-}15\text{ km}$, uses a global mesh that varies in resolution by a factor of ~ 5 ($x5$) with a 15 km resolution in the North Atlantic (NA) and 80 km elsewhere. The last simulation, $x5\text{-}NA\text{-}7.5\text{ km}$ uses 7.5 km resolution in the NA and approximately 40 km resolution elsewhere. The validity of the modeling approach when configured with a global, quasi-uniform resolution is evaluated by comparing the $x1\text{-}15\text{ km}$ simulation to observational estimates of mean and variance of sea-surface height, as well as analysis of volume transports across well-documented sections. The validity of the multi-resolution modeling approach is evaluated by comparing the $x5\text{-}NA\text{-}15\text{ km}$ simulation to the $x1\text{-}15\text{ km}$ simulation in the NA region. While the $x1\text{-}15\text{ km}$ simulation certainly has errors as compared to observations, the error in the multi-resolution approach is measured by comparing a variable resolution simulation to its quasi-uniform counterpart. Therefore, a “perfect” multi-resolution simulation will reproduce both the positive and negative results of its quasi-uniform counterpart within the high-resolution region. The $x5\text{-}NA\text{-}7.5\text{ km}$ simulation serves to motivate one potential benefit of this modeling approach as it requires approximately the same computational expense, including the cost of a reduced time step, as the $x1\text{-}15\text{ km}$ simulations, but redistributes the computational degrees of freedom to obtain higher resolution in the NA.

Section 2 provides an overview of the meshes used in this study. More importantly, Section 2 discusses the underlying properties of these meshes that have led us to choose them over more traditional options. Section 3 provides a high-level summary of the numerical approaches used to construct this global ocean model. Since many of these methods are commonly employed in global ocean modeling, the discussion is primarily meant to highlight how this ocean model compares and contrasts with current IPCC-class ocean models. A detailed derivation of the model equations is discussed in Appendix A. Section 4 provides specific details used in the simulations that are then discussed in Section 5. We close in Section 6 with a summary of what has been accomplished with this contribution and what remains to be done.

2. Multi-resolution tessellations of the global ocean

The novel aspect of this contribution is the ability to model the global ocean system using a high-quality, yet easy-to-construct, multi-resolution tessellation (aka mesh or grid). High-quality refers to high local uniformity while multi-resolution refers to the presence of multiple scales. While the attributes of local-uniformity and multi-resolution might seem at odds, the meshes described below have both of these properties. As such, we begin by introducing the relevant aspects of these multi-resolution meshes and describe how such meshes are constructed. While

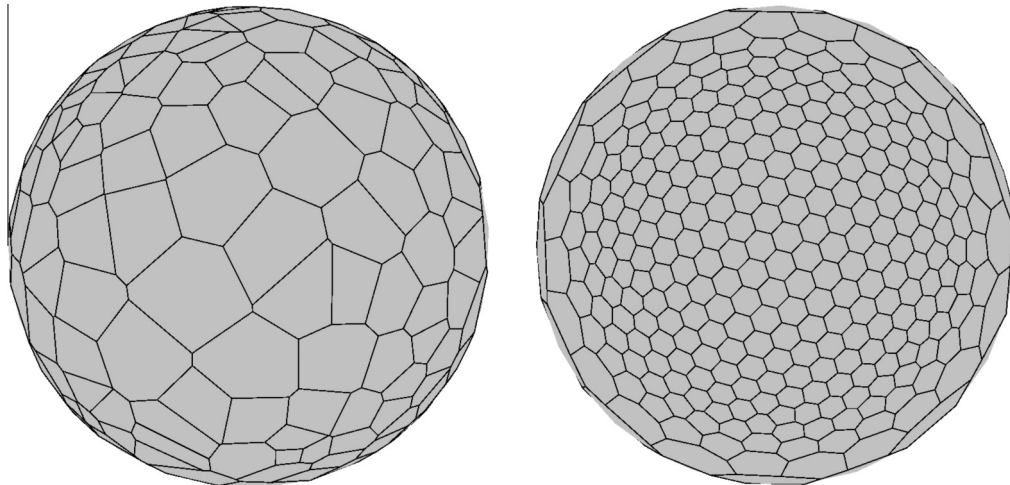


Fig. 1. These are examples of Voronoi tessellations. The mesh on the left is created by randomly distributing 366 points on the surface of the sphere and determining the Voronoi regions following (1). The mesh on the right begins as the mesh on the left, but moves the points on the sphere via iteration such that (2) is also satisfied.

the numerical method to be described below can be employed on a wide range of conforming meshes, our clear preference is to use Spherical Centroidal Voronoi Tessellations (SCVTs). Descriptions of SCVTs and their mathematical properties has been discussed at length in the literature. So our purpose here is only to review the most salient aspects of SCVTs, while providing references to both the seminal and more recent discussions of these grids.

We begin with a description of a Voronoi tessellation, then move to a discussion of SCVTs that are a special subset. For the moment, let us assume that we wish to tessellate the entire surface of the sphere, S , with n cells. We start by populating S with $\{\mathbf{x}_i\}_{i=1}^n$ distinct grid points. We then assign every point on the sphere to whichever \mathbf{x}_i it is closest to. This results in a set of Voronoi regions, $\{V_i\}_{i=1}^n$, where each region (or cell) is uniquely associated with a single grid point. Mathematically, this can be expressed as

$$V_i = \{\mathbf{y} \in S \mid \|\mathbf{x}_i - \mathbf{y}\| < \|\mathbf{x}_j - \mathbf{y}\| \text{ for } j = 1, \dots, n \text{ and } j \neq i\}. \quad (1)$$

An example of a Voronoi tessellation on the sphere can be found in Fig. 1 (left). Ju et al. (2010) provide a concise summary of the history of Voronoi tessellations and their eventual use in climate modeling, whereas Okabe et al. (2009) provide a complete survey of the history, mathematics and application of these tessellations. Algorithms for the construction of Voronoi diagrams are mature and discussed in Renka (1997) and Okabe et al. (2009).

A Voronoi tessellation is the dual-mesh of a Delaunay triangulation; specifying either uniquely determines the other. The meshes are dual in the sense that the vertices of one mesh are the centers of the other mesh.¹ This duality also extends to the notion of orthogonality. The line segment connecting two $\{\mathbf{x}_i\}$ points that share an edge is orthogonal to that shared edge. This property of orthogonality is critical to the numerical method that is built “on top” of these meshes (Thuburn et al., 2009; Ringler et al., 2010). While Voronoi tessellations have a few compelling attributes, the mesh shown in Fig. 1 (left) is clearly not optimal for numerical modeling. We regularize this Voronoi tessellation by requiring that each grid point be the centroid of its Voronoi region with respect to a user-defined mesh-density function. Thus, we require

$$\mathbf{x}_i = \mathbf{x}_i^c = \frac{\int_{V_i} \mathbf{y} \rho(\mathbf{y}) d\mathbf{y}}{\int_{V_i} \rho(\mathbf{y}) d\mathbf{y}} \quad (2)$$

¹ This sense of duality can be seen in Fig. 3, where the hexagon is a Voronoi region and the triangle is a Delaunay region.

where ρ is the user-defined mesh-density function. Eq. (1) with the constraint of (2) results in an iterative procedure. The Voronoi regions depend on the location of the grid points (as shown in (1)), but the location of the grid points depend on the region of integration (as shown in (2)). Fortunately, a host of methods exist to efficiently solve this system iteratively (Lloyd, 1982; Ju et al., 2002; Jacobsen et al., 2013).

These Centroidal Voronoi Tessellations (CVTs) and their spherical counterparts, SCVTs, both regularize the Voronoi tessellation and provide a powerful degree of freedom through the specification of the mesh-density function. For example, Fig. 1 (right) shows an SCVT where the mesh density function has large values in the center and low values elsewhere. Note that the iterative procedure used to produce Fig. 1 (right) starts from Fig. 1 (left). The mathematical analysis of (S)CVTs was reinvigorated by Du and Gunzburger (1999) who showed that these tessellations are often optimal solutions to a wide range of important problems, such as data compression, quadrature rules, finite-difference schemes and resource allocation.

From the perspective of global ocean modeling, two properties of (S)CVTs are noteworthy. The first property is the known relationship between the (input) mesh-density function and the (output) grid resolution (Ju et al., 2010). On the plane or sphere, this relationship is stated as

$$\frac{dx_i}{dx_j} \approx \left(\frac{\rho(\mathbf{x}_j)}{\rho(\mathbf{x}_i)} \right)^{\frac{1}{d}}, \quad (3)$$

where dx is the nominal grid resolution as measured by the distance between neighboring \mathbf{x}_i points. Eq. (3) states that given ρ and the grid resolution at any one location, we know the grid resolution at every point in the domain. Fig. 2 in Ringler et al. (2011) demonstrates that this relationship holds with a high level of accuracy. The practical implications of (3) is that we can build our mesh density function to produce the desired grid resolution in each part of the ocean domain. Fig. 1 (right) uses a simple mesh-density function expressed as

$$\rho(\mathbf{x}_i) = (1 - \gamma) \left[\frac{1}{2} \left(\tanh \left(\frac{\beta - \|\mathbf{x}_c - \mathbf{x}_i\|}{\alpha} \right) + 1 \right) \right] + \gamma \quad (4)$$

where β measures the width of the high-resolution region, α defines the width of the mesh transition zone, \mathbf{x}_c denotes the center of the high-resolution region and γ controls the ratio between the nominal grid spacing in the high and low resolution regions. For the variable resolution meshes used in this study, we set $\beta = 0.628$ radians,

$\alpha = 0.1$ radians, $\mathbf{x}_c = (310^\circ, 35^\circ)$ and $\gamma = (1/6)^4$. In general, we specify $0 < \rho \leq 1$ where $\rho \approx 1$ corresponds to the high-resolution region and $\rho \approx \gamma$ corresponds to the low-resolution region. With this convention, the ratio between grid resolutions in the high and low resolution regions can be obtained as $\gamma^{\frac{1}{4}}$. So with γ set to $(1/6)^4$, we expect to obtain meshes that vary in resolution by $6\times$. As will be seen below, the resulting meshes vary in resolution by a little more than $5\times$. This difference between the theoretical estimate of $6\times$ and the result of $5\times$ is an indication of the level of precision offered by the underlying theory. More exotic choices of mesh-density function are possible, for example see Figs. 7–9 of Ringler et al. (2008). The rate of change of mesh resolution is controlled by $\nabla\rho$. As is demonstrated below, the density function (4) used for this study results in an extremely smooth mesh transition zone. Sharper mesh transitions zones are certainly possible, but the upper bound of $\nabla\rho$ will depend on the numerical method.

The second noteworthy property is known as the “hexagon theorem” proven independently by Gershoff (1979) and Newman (1982). The theorem states that given minimal constraints on ρ , such as continuity, the preferred polygon is a perfect hexagon. Stated alternatively, as the number of grid points in the domain is increased while holding ρ fixed, the mesh evolves toward a set of perfect hexagons. The practical result of this theorem is that for a given mesh-density function, the local mesh uniformity increases as the number of grid points are increased. Thus, meshes are guaranteed to improve in quality as resolution is increased. Ample anecdotal evidence for this can be found in Tables 1–3 of Ringler et al. (2008).

In summary, SCVTs offer precise control over the distribution of grid points with the promise of high mesh quality as the number of grid points increases. These two reasons, as well as the isotropy of the hexagon relative to quadrilaterals and triangles, lead us to build the ocean dynamical core “on top” of SCVTs.

To this point we have only discussed the construction of meshes that cover the entire sphere. Currently we produce global ocean meshes by simply culling those Voronoi regions that reside mostly over land. While this is the common approach for ocean global models, it is not optimal. SCVTs offer the opportunity to fit the mesh to the land–ocean boundary and/or continental shelf break, as shown in Fig. 10 of Ju et al. (2010). While we are not exploiting this attribute of SCVTs, we expect that doing so will lead to improved simulations, as well as the opportunity to better represent coastal ocean dynamics.

This study employs three meshes, as summarized in Table 1. The first simulation, $x1\text{-}15\text{ km}$, uses 1.8×10^6 grid points with a uniform density function $\rho = 1$, resulting in a quasi-uniform, global ocean mesh with a nominal resolution of 15 km. This mesh contains 1.9×10^5 grid points, or approximately 10% of the mesh, within the NA, i.e. within a distance β from \mathbf{x}_c . The next mesh, $x5\text{-NA}\text{-}15\text{ km}$, is constructed using (4). This mesh contains a total of 2.5×10^5 grid points, with 70% of those grid points located in the NA. The $x1\text{-}15\text{ km}$ and $x5\text{-NA}\text{-}15\text{ km}$ meshes have nearly the same resolution in the NA, about 15.1 and 15.8 km respectively,

and so are used to compare the uniform versus the variable resolution mesh simulations.

The two variable resolution meshes, denoted as $x5\text{-NA}\text{-}15\text{ km}$ and $x5\text{-NA}\text{-}7.5\text{ km}$, are meant to demonstrate a new opportunity in global ocean modeling. The $x5\text{-NA}\text{-}15\text{ km}$ simulation requires approximately 1/7 the computational resources of the $x1\text{-}15\text{ km}$ simulation, but retains the same resolution in the NA. Thus, the $x5\text{-NA}\text{-}15\text{ km}$ simulation offers the potential to obtain eddy-permitting solutions of the NA at a fraction of the computational cost. Alternatively, the $x5\text{-NA}\text{-}7.5\text{ km}$ simulation uses approximately the same resources as the $x1\text{-}15\text{ km}$ simulation,² thus offering modelers the opportunity to reallocate a fixed amount of computational resources into a specific region in order to better represent a process of interest.

The top graphic in Fig. 2 shows the mesh density function, where red indicates the region of high resolution, purple indicates the region of low resolution and green indicates the mesh transition zone. Regions of this mesh are also shown in Fig. 2. The graphic on the left expands the mesh in the region of the Florida Straits to a scale where individual grid cells are visible. The graphic on the right expands a region of the mesh transition zone. We note that even in the mesh transition zone, the mesh is smooth and locally uniform.

3. Numerical approach

The approach employs variations of well accepted numerical methods to obtain multi-resolution representations of the global ocean system. We employ a finite-volume discretization of the Boussinesq equations using a C-grid staggering in the horizontal (Thuburn et al., 2009; Ringler et al., 2010), a z^* vertical coordinate (Adcroft and Campin, 2004), a split-explicit time stepping algorithm (Higdon, 2005), a quasi 3rd-order monotone advection scheme for tracers (Skamarock and Gassmann, 2011) and the Leith, enstrophy-cascade turbulence closure (Leith, 1996). The goal of this section is to broadly discuss these parts of the global ocean model, with an emphasis on the horizontal discretization since this is not currently employed in existing global or coastal ocean models. Specific details related to the numerical approach are discussed in Appendix A.

3.1. Horizontal discretization

The horizontal discretization (detailed in Appendix A.4) is a C-grid, finite-volume method that is applicable to a broad class of meshes. Issues related to geostrophic balance and geostrophic adjustment are analyzed by Thuburn et al. (2009) in the context of the linearized shallow-water equations. The analysis of the non-linear shallow-water system is conducted in Ringler et al. (2010) where issues related to mass, potential vorticity and energy conservation are discussed. The staggering of variables shown in Fig. 3 is essentially the C-grid staggering as expressed on an SCVT mesh where the mass, tracers, pressure and kinetic energy are defined at centers of the convex polygons and the normal component of velocity is located at cell edges. As with all C-grid staggered models, the divergence of velocity is defined at cell centers and the curl of velocity is defined at cell vertices.

The properties of this C-grid discretization are consistent with the requirements of global ocean simulation on time scales of decades to centuries. By virtue of retaining a volume conservation equation and prognosing volume-weighted tracer quanti-

² The $x5\text{-NA}\text{-}7.5\text{ km}$ simulation use 1/2 the grid cells but also about 1/2 the time step as compared to the $x1\text{-}15\text{ km}$ simulation, thus resulting in both simulations requiring approximately the same amount of computational resources.

Table 1

Summary of meshes used in simulations: Three meshes are used in the global ocean simulations. The $x1\text{-}15\text{ km}$ mesh has approximately 15 km resolution throughout the ocean. The $x5\text{-NA}\text{-}15\text{ km}$ simulation has approximately 15 km resolution in the NA region and 80 km elsewhere. The $x5\text{-NA}\text{-}7.5\text{ km}$ has approximately 7.5 km resolution in the NA and 40 km resolution elsewhere.

Simulation name	Grid cells	Grids cells in NA	Resolution (km)
$x1\text{-}15\text{ km}$	1.8×10^6	1.9×10^5	~15, ~15
$x5\text{-NA}\text{-}15\text{ km}$	2.5×10^5	1.7×10^5	~80, ~15
$x5\text{-NA}\text{-}7.5\text{ km}$	1.0×10^6	6.7×10^5	~40, ~7.5

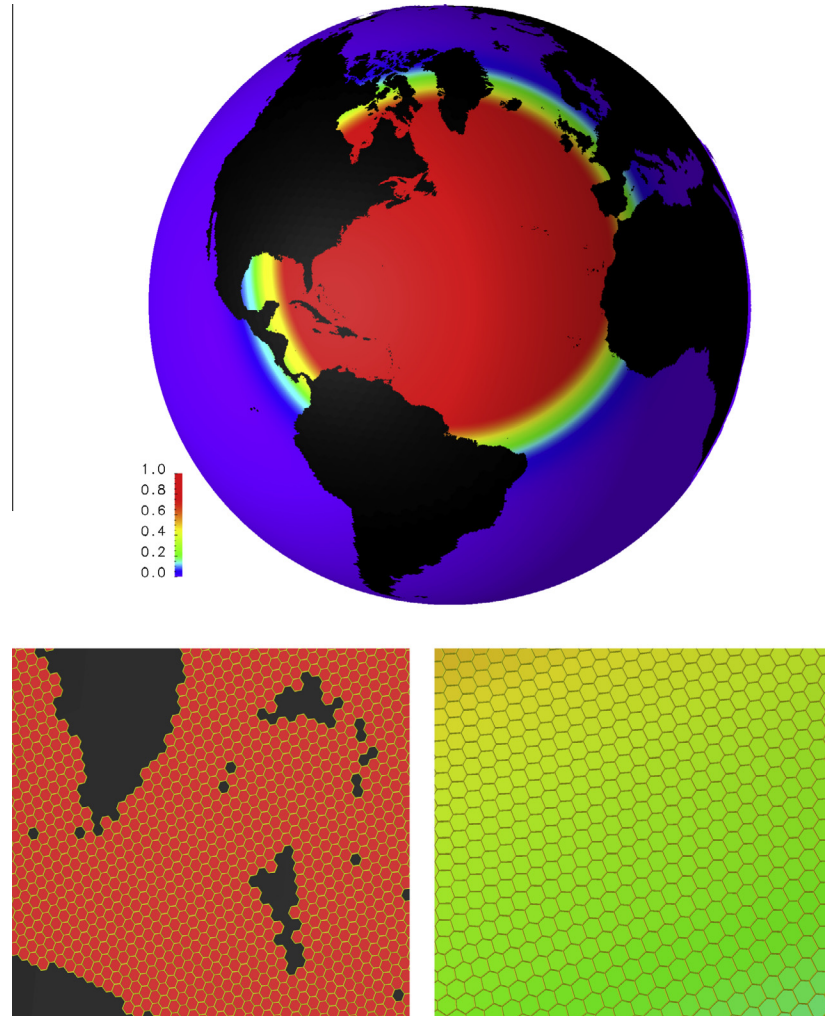


Fig. 2. This figure summarizes the quality and characteristics of the multi-resolution meshes. The top figure shows the mesh density with red values indicating $\rho \approx 1$ and blue values indicating $\rho \approx \gamma$. The lower left and right panels expand a portion of the mesh in the vicinity of the Florida Straits and tropical Atlantic, respectively. We note that both the lower panels exhibit a very uniform mesh composed entirely of near-regular hexagons. (For interpretation of the references to colour in this figure legend, the reader is referred to the web version of this article.)

ties, the method guarantees conservation of volume and volume-weighted tracer substance. Extending this formulation to a non-Boussinesq system is trivial. In terms of energetics, the Coriolis force is computed so that it is energetically neutral (see Section 3 of Thuburn et al., 2009), and exchange of kinetic and potential energy is conservative (see (70) of Ringler et al., 2010). In terms of vorticity, the curl of the discrete momentum equation produces a discrete absolute vorticity equation where circulation is conserved within closed loops moving along Lagrangian trajectories, i.e. the method includes a discrete analog of Kelvin's circulation theorem (see (35) of Ringler et al., 2010).

This method can be regarded as a generalized C-grid discretization in the sense that the method holds for any conforming mesh composed of convex polygons that are locally-orthogonal. The requirement of conforming simply means that every edge of the mesh is uniquely shared by two grid cells. The requirement of locally-orthogonal means that the line segment connecting two grid points is orthogonal to their shared edge. It turns out that a very large number of meshes meet these requirements: latitude-longitude grids, dipole and tripole displaced pole grids, conformally-mapped cubed sphere grids, Voronoi tessellations and Delaunay triangulations.

The novel aspect of this C-grid algorithm is that its mimetic properties are unaltered when configured on a multi-resolution mesh. In a very real sense, it is the combination of the mesh technology outlined in Section 2 paired with this generalization of the C-grid method that allows the exploration of global, multi-resolution ocean modeling. In the context of the shallow-water equations, Ringler et al. (2011) verified the robustness of this approach by configuring the Williamson (1992) test case suite with meshes that varied by up to a factor of 16 in grid spacing. All of the conservation properties were confirmed using the shallow-water test cases. This same numerical approach has been used to construct full-physics atmosphere general circulation models based on the hydrostatic (Rauscher et al., 2013) and non-hydrostatic (Skamarock et al., 2012) primitive equations.

3.2. Vertical discretization

The vertical coordinate is Arbitrary Lagrangian–Eulerian (ALE), which provides a great deal of freedom to specify the behavior of the vertical coordinate that is most appropriate for the application. The user may choose at run-time among z-level, where all layers have a fixed thickness except for the top layer; z^* , where all layer thicknesses compress in proportion to the sea surface height

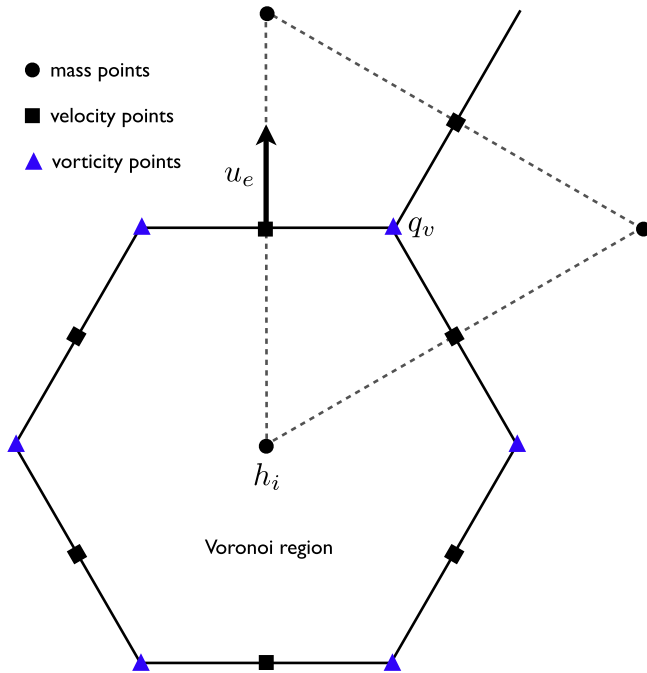


Fig. 3. The staggering of variables for the generalized C-grid method. The Voronoi region represents a typical finite-volume cell where scalars, such as thickness (h_i), are defined. The component of velocity normal to the cell edges (u_e) is predicted. The divergence of this component of velocity is naturally defined at mass points, whereas the curl of this velocity is naturally defined at the vertices (q_v) of the Voronoi region.

(Adcroft and Campin, 2004); z-tilde, where thicknesses respond to high-frequency oscillations in a Lagrangian manner (Leclair and Madec, 2011); and idealized isopycnal,³ where there is no vertical transport between layers. The choice of vertical coordinate is enforced in the computation of the vertical transport, while the prognostic equation for layer thickness is solved in the same manner in all cases (see Appendix A.3 for a detailed discussion).

The simulations presented here use a z^* vertical coordinate. Advantages include reduced spurious vertical mixing due to surface gravity waves; layers may be extremely thin to better resolve mixed layer dynamics; and future simulations may easily accommodate partially submerged ice shelves and embedded sea ice. These simulations used 40 vertical layers ranging in thickness from, on average, 10 m at the surface to 250 m at depth with a maximum ocean depth of 5500 m. Bathymetry is accounted for using land-filled full cells that prohibit fluid advection at horizontal and vertical boundaries.

3.3. Temporal discretization

All modern ocean models take advantage of a baroclinic/barotropic time-splitting method to increase the time-step length and hence increase computational efficiency. The time step for the two-dimensional barotropic mode is limited by fast surface gravity waves with speeds of ~ 200 m/s, while the remaining three-dimensional baroclinic system is limited by slow internal waves with speeds of ~ 1 m/s. We use a split explicit method (see Appendix A.5), where the barotropic (thickness-weighted vertical average) velocity and total ocean depth are explicitly subcycled within each large time step of the three-dimensional baroclinic velocity. The time stepping algorithm is loosely based on Higdon (2005). The full

tracer and thickness equations are stepped forward with the mid-time velocity values, and density and pressure are updated at the end of the time step. This whole process is repeated in a predictor–corrector scheme, and implicit vertical mixing of tracers and momentum completes each time-step.

3.4. Tracer transport

The transport equation of potential temperature and salinity (A.41) is expressed in flux-form, in that our prognostic equation is for volume-weighted tracer substance.⁴ Tracer values (e.g. potential temperature) are recovered by dividing by the volume of the grid cell at the end of every time step. Tracer transport is completed at the end of the time step, so the volume flux across every edge is known. Thus, the tracer transport algorithm reduces, in large part, to reconstructing the tracer fields at cell edges, in that determining the $\hat{\varphi}$ shown in A.41. We obtain two estimates of the tracer edge values, one from a high-order flux reconstruction and one from a low-order flux reconstruction.

In the horizontal, the high-order flux reconstruction is done following Skamarock and Gassmann (2011) where, at a given edge, the tracer field is approximated by averaging the Taylor series approximations from both cells that share that edge (see (11) from Skamarock and Gassmann, 2011). Since the edge is exactly midway between the cells centers, all odd-powered derivatives cancel and, thus, only second derivative information in the direction normal to the cell edge is required. The second derivative information is obtained by first computing a least squares fit using the cell center values and all distance-1 neighbors (i.e. all neighbors that share an edge with the cell center, see Fig. 1 from Skamarock and Gassmann, 2011). The scheme is implemented with an upwind-bias ($\beta = 0.25$ in (11) from Skamarock and Gassmann, 2011) to produce a 3rd-order accurate reconstruction of tracer flux divergence on uniform hexagonal meshes with a constant velocity. In the vertical, high-order estimates of tracer values at layer edges are reconstructed using a 3rd-order cubic spline. While the 3rd-order flux reconstructions improve the accuracy of the transport scheme, the Skamarock and Gassmann (2011) scheme exhibits 2nd-order spatial convergence because the flux-divergence operator remains 2nd-order accurate. The low-order reconstruction, in both the horizontal and vertical directions, is simply the upstream cell center value. These two estimates of the tracer at cell edges are used to produce a high- and low-order estimate of the tracer flux. We then use the flux-corrected transport scheme of Zalesak (1979) to blend the high- and low-order fluxes to yield a monotonic evolution of the tracer field.

3.5. Horizontal turbulence closures

The constraint of monotonicity in the transport of potential temperature and salinity is sufficient to regularize the evolution of these scalar quantities. Thus, no additional explicit diffusion is required for the potential temperature and salinity fields, unless needed to represent unresolved physical processes. In contrast, the velocity field is not evolved based on flux-form discretization and, therefore, requires an explicit closure to prevent the build up of grid-scale kinetic energy and enstrophy. We use two methods to regularize the momentum equation: biharmonic viscosity and the Leith turbulence closure.

Biharmonic viscosity is a standard method for controlling grid scale noise in the velocity. Following Smith et al. (2000) and Hecht et al. (2008), we scale the biharmonic viscosity parameter as $(\Delta x)^3$,

³ “Idealized isopycnal” implies that all isopycnal layers have non-zero thickness.

⁴ In the Boussinesq system, conservation of density-weighted tracer substance reduces to conservation of volume-weighted tracer substance.

with a baseline value of $5.0 \times 10^{-4} \text{ m}^4/\text{s}$ at a grid spacing of 15 km. When scaled to adjust for resolution, this value of biharmonic viscosity is a factor of 2 to 10 less than that used in Hecht et al. (2008).

Our preference in configuring these simulations is to use the smallest value of biharmonic viscosity sufficient to control grid scale noise in the velocity field and rely on the Leith turbulence closure (Leith, 1996) to remove the downscale cascade of enstrophy. The Leith closure is the enstrophy-cascade analogy to the Smagorinsky (1963) energy-cascade closure, i.e. Leith (1996) assumes an inertial range of enstrophy flux moving toward the grid scale. The assumption of an enstrophy cascade and dimensional analysis produces right-hand-side dissipation, \mathbf{D} , of velocity of the form

$$\mathbf{D}_h^u = \nabla \cdot (v_h \nabla \mathbf{u}) = \nabla \cdot (\Gamma |\nabla \omega| (\Delta x)^3 \nabla \mathbf{u}) \quad (5)$$

where ω is the relative vorticity, \mathbf{u} is the horizontal velocity, Δx is the local grid spacing and Γ is a non-dimensional, $O(1)$ parameter. In the simulations presented below, we set $\Gamma = 1$.

While the Leith closure is used much less often than the Smagorinsky closure, the Leith closure has shown promise when the grid resolution permits mesoscale eddies (Fox-Kemper and Menemenlis, 2008). In addition, an evaluation of the Leith closure in idealized, 2D turbulence simulations indicates that this closure is competitive with other LES closures (Pietarila Graham and Ringler, 2013).

Vertical viscosities and diffusivities were computed using the Richardson number formulation of Pacanowski and Philander (1981) with background values of 10^{-4} and $10^{-5} \text{ m}^2/\text{s}$, respectively. As stated above, the vertical mixing is solved implicitly, thus allowing the large values of viscosity and diffusivity of $1.0 \text{ m}^2/\text{s}$ to be used in regions that are gravitationally unstable.

4. Design of numerical experiments

4.1. Initial and boundary conditions

The land/sea boundary and bathymetry for each simulation (listed in Table 1) are obtained by interpolation of the ETOPO2 2-Minute Gridded Global Relief Dataset available from the National Geophysical Data Center. Given a global mesh (e.g. a higher resolution version of the mesh shown in Fig. 1 (right)), we loop over all grid cells and, for each grid cell, we find the nearest ETOPO2 data point. If the ETOPO2 data point has a positive elevation, the grid cell is marked as land and culled from the mesh. If the ETOPO2 data point has a negative elevation, then the grid cell is marked as ocean and retained. The depth of each ocean column is specified to be the nearest full-level interface to the ETOPO2 data point, i.e. partial bottom cells (Adcroft et al., 1997) are not included in these simulations. Note that alternative strategies of averaging ETOPO2 data over the ocean grid cell will result in smoother representations of bathymetry. We require each ocean column to contain at least three vertical levels. This approach specifies the ocean domain. Note that the ocean model domain is composed of a set of full grid cells. As a result, the land-sea boundary is defined by a set of cell edges, as can be seen in the lower left panel of Fig. 2. As described above, the velocity is defined at cell edges. At all edges that lie along the boundary of the ocean domain, we employ a no-slip boundary condition on the velocity field.

Initial distributions of potential temperature and salinity are obtained from the annual mean WOCE climatology (Gouretski and Koltermann, 2004). For simplicity, the sea surface temperature (SST) and salinity (SSS) are restored to the monthly mean WOCE surface data with a time scale of 30 days in the simulations presented below. For the surface momentum flux, monthly mean wind stress is computed offline using 6-hourly “Normal Year” forcing data from the Coordinated Ocean-ice Reference Experiment

(CORE, Large and Yeager, 2004) and bulk formulae of Large and Pond (1982). At any given day, the model obtains the restoring SST and SSS along with the imposed wind-stress by linearly interpolating between the monthly forcing data sets. No modifications are made to account for sea-ice coverage.

The simulations are started from rest and integrated for 20 simulated years. Since a decade is sufficient to reach a quasi-equilibrium for many important features of the upper ocean circulation, the first 10 years are discarded as spin-up. All results that refer to time-mean or variance calculations imply the use of the last 10 years of simulation. Variance and Root Mean Square (RMS) calculations are computed based on instantaneous snapshots of the model state sampled once every 10 days after removing the time-mean state.

5. Results

5.1. Comparison of global, eddy-permitting simulation to observations

Before comparing the $x1\text{-}15 \text{ km}$ simulation to observational datasets, we begin with a brief survey of the kinetic energy (KE) field at a depth of 100 m as shown in Fig. 4. This figure shows a representative snapshot of the global KE field for October 1st of Year 15. The color scale is saturated to red for velocities at 1.0 m/s. Beginning in the tropics, the Pacific contains a strong equatorial undercurrent with extended sections above 1.0 m/s. Tropical Instability Waves (TIWs) are present with a wavelength of approximately 1000 km, which is consistent with observations (Legeckis, 1977). The TIWs begin to grow each July, reach maximum amplitude in November and then decay in January. In the Atlantic the equatorial undercurrent is also present, with velocities generally below 1.0 m/s. As observed, the Atlantic equatorial undercurrent is fed via retroflection of the north Brazil current, which periodically sheds coastally trapped rings that propagate into the Caribbean.

Moving into the midlatitudes, the $x1\text{-}15 \text{ km}$ simulation exhibits the shedding of Agulhas Rings with a frequency of 4 or 5 per year, which is consistent with observations (Schouten et al., 2002). While the frequency is approximately correct, the vortex rings are too long-lived with their coherent structure maintained even after reaching the South American coast. The track of the Agulhas rings is approximately correct; the rings move in a northwest direction immediately after shedding, then turn to move almost directly west between latitudes of 20°S and 25°S . However, almost all of the rings are locked into a similar path, which is not the case in the real ocean, though is not uncommon in models (e.g., McClean et al., 2011). The location of retroflection of the Agulhas Current is variable, sometimes extending west beyond Cape Agulhas. Further north along the East African coast, the simulation reproduces the seasonality of the Indian Ocean currents with the boreal summer occurrence of the Giant Whirl as seen in Fig. 4 at $5^\circ\text{N}\text{--}60^\circ\text{E}$ and the boreal winter intensification of the South Equatorial Counter-current (not shown).

Elsewhere in the Southern Hemisphere mid-latitudes, the $x1\text{-}15 \text{ km}$ simulation exhibits vortex ring shedding in the region off west Australia. The shedding is spawned from both the Leeuwin Current (Fang and Morrow, 2003) and Flinders Current (Middleton and Cirano, 2002) during the austral winter when these currents intensify. The rings move westward into the south Indian Ocean subtropical gyre and decay before reaching the African coast.

The dominant feature in the Southern Ocean is the highly filamented Antarctic Circumpolar Current (ACC). Locations of the major fronts, such as the Sub-Antarctic Front (SAF) and the Polar Front (PF) are clearly reflected in the 100 m KE. The westward Antarctic

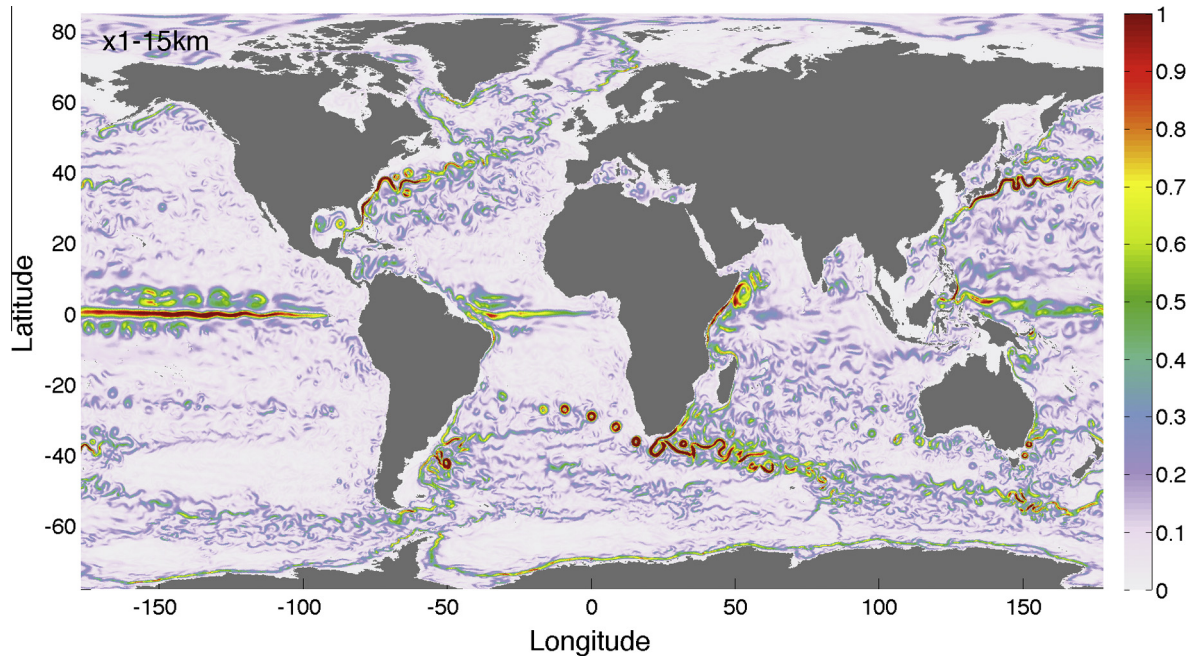


Fig. 4. A snapshot of velocity magnitude on October 1st Year 15 at a depth of 100 m for the *x1-15 km* simulation. The color scale saturates at red where instantaneous velocities reach 1.0 m/s. (For interpretation of the references to colour in this figure legend, the reader is referred to the web version of this article.)

Coastal Current can also be seen just offshore of the Antarctic continent at all longitudes.

In the northern Hemisphere both the major western boundary currents exhibit delayed separation by, on average, approximately 300 km. The orientation of the Kuroshio is appropriate with the axis oriented east–west. As will be discussed in more detail below, the axis of maximum Gulf Stream variability is rotated about 10° counter clockwise relative to observations. Moving polewards in the Atlantic basin, the East and West Greenland currents are present with a clear connection to the Labrador Current.

A closer examination of the structure of the equatorial currents is shown in Fig. 5. The left panels show zonal flow through a meridional section at 140°W from the (bottom) *x1-15 km* simulation and (top) observations (Johnson et al., 2002). The right panels show zonal flow along the equator. The Equatorial Undercurrent (EUC) has the correct velocity of ~1.0 m/s at a depth that is ~20 m too shallow. The North Equatorial Counter Current (NECC) has an amplitude only half as large as observed and is shifted ~1° equatorward. In addition, the NECC has a subsurface maximum that is not seen in the observations. Both the North and South Subsurface Countercurrents are present with the correct depth of 300 m, amplitude of 0.1 m/s and location of ~4° latitude. The model also captures the Equatorial Intermediate Current (EIC) at a depth of 300 m with an amplitude of 0.1 m/s. Relative to observations the EIC is shifted east and, thus, has a larger amplitude at 140°W than the observed estimate. The eastward shift of the EIC is readily visible in the longitudinal sections shown to the right. The primary bias along the equator is that the simulated EUC does not exhibit the appropriate amount of upward tilt toward the east. We attribute this bias to an insufficient amount of downward mixing of westward momentum between 175°W and 125°W. Overall, the model compares favorably with observations and to other models of comparable resolution, e.g. Fig. 11 of Maltrud and McClean, 2005.

In Fig. 6 the time-mean, global SSH from the *x1-15 km* simulation is compared to the Maximenko et al. (2009) dataset which merges Gravity Recovery and Climate Experiment (GRACE) data with observations of near-surface velocity to estimate the mean

dynamic topography. All of the large-scale gyres are represented in the *x1-15 km* simulation, but with amplitudes that are larger than those found in the Maximenko et al. (2009) dataset. The difference plot (Fig. 6, bottom) indicates that the subtropical gyres exhibit peak SSH amplitudes that are typically too large by 0.25 to 0.40 m as compared to the observations. Overall, the structure of SSH shown in Fig. 6 closely follows Fig. 8c of McClean et al. (2011) that shows the mean SSH from POP when forced with the same wind-stress as used in the *x1-15 km* simulation. The subtropical gyre in the North Pacific, while too large in amplitude, has the correct latitudinal extent. The subpolar front on which the Kuroshio current resides is shifted poleward approximately 300 km but has the correct east–west orientation. The South Pacific subtropical gyre is of approximately the correct amplitude, but shows a banded structure in the meridional direction that is not found in the observations. Again, this is most likely due to the applied wind stress since a similar pattern is seen in POP simulations that use the same monthly stress field (McClean et al., 2011, Fig. 8c). As compared to observations, a large discrepancy in SSH occurs just equatorward and east of New Zealand. In this region the *x1-15 km* simulation maintains a strong, east–west oriented subtropical front that has no analog in the observations. The largest discrepancy in the region of the ACC is the maximum SSH amplitude of the Argentine subpolar gyre. In the region of the Agulhas current, the westward extension of the subtropical gyre is well simulated but with frontal structures that are too strong. The impact of the excessive mesoscale activity and the very regular path of the Agulhas Rings is evident even in the mean SSH, with the *x1-15 km* simulation supporting a weak northwest–southeast oriented front along the mean trajectory of these coherent eddies. The model simulates well the frontal boundary in the region of Madagascar that connects the South Equatorial Current to the East African Coastal Current. We defer a discussion of the simulation in the NA until the next section.

The global SSH RMS from the *x1-15 km* simulation is compared to the AVISO dataset in Fig. 7. Overall, each of the major areas of significant mesoscale eddy activity are represented in the *x1-15 km* simulation. In addition, the amplitude of the mesoscale activity

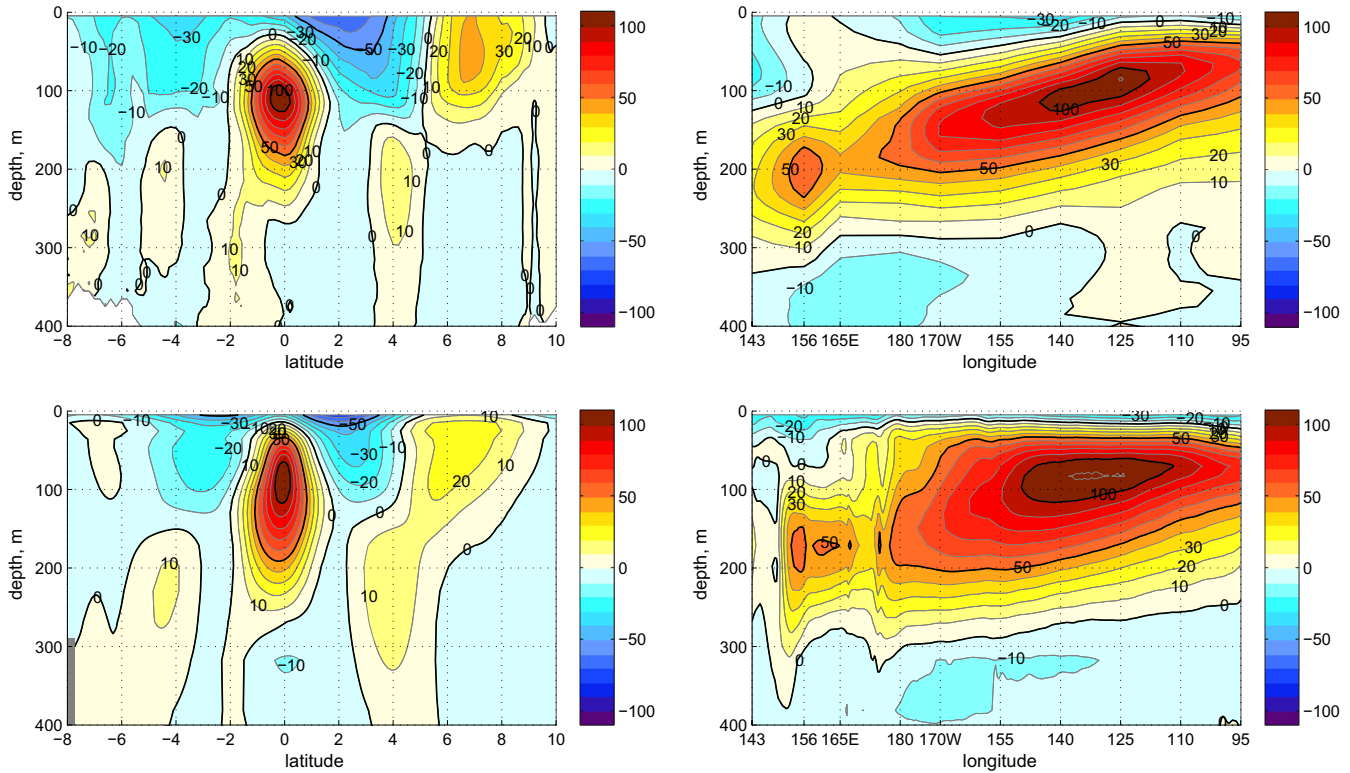


Fig. 5. Cross section of zonal velocity from observations (top) and from the $x1\text{-}15\text{ km}$ simulation (bottom) at 140°W (left) and the equator (right). Contour interval is 10 cm s^{-1} with heavy contours at 50 cm s^{-1} . Observations are averaged over multiple studies from 1985 to 2000 (Johnson et al., 2002).

in those major regions is, in general, accurately represented in the simulation. For example, SSH variance has the correct amplitude in the region of the Kuroshio, but is shifted polewards by approximately 300 km as is consistent with the biases identified in mean SSH. The eddy activity in the regions of the East Australia Current, Drake Passage and Argentine Basin is in close agreement with the AVISO dataset with respect to both structure and amplitude. The anomalous frontal structure residing northeast of New Zealand that is discussed above is clearly reflected in Fig. 7. There is also vigorous shedding of vortex rings from West Australia that migrate well into the South Indian Ocean. The SSH variance in the Agulhas Current along its coastal extent and in the retroflection region is well represented in both shape, but is too strong in magnitude after retroflection. Again, the Agulhas Rings are too strong and follow too regular of a path, thus resulting in too much variance of SSH along their trajectory across the South Atlantic. As above, we defer a discussion of the simulation in the NA until the next section.

The transports of some of the major current systems are shown in Table 2. While transports for all three simulations are listed in Table 2, we will defer discussion of the variable resolution simulations until the next section. The observed transports are listed with the best estimate along with an estimate of observational error. The simulated transports are listed with a mean transport along with the standard deviation. The $x1\text{-}15\text{ km}$ simulation is broadly reproducing the observed transports, meaning that the simulated mean transports plus/minus one standard deviation are all within observational error. As is typically the case for ocean models, those currents associated with intense mesoscale activity are stronger than observed, e.g. the simulated transports of Drake Passage, Tasmania-Antarctica and Agulhas are all larger than observed. On the other hand, the simulated transports of tropical current systems and/or current systems that are sensitive to channel configuration are all weaker than observed, e.g. the simulated transports of the Indonesian Throughflow and Mozambique Channel. In these simu-

lations, ocean depth is taken directly from the ETOPO2 topography data without widening or deepening channels in order to improve transport statistics.

5.2. Comparison of global, multi-resolution simulations to global, quasi-uniform simulation

One of the main questions to be addressed in this contribution is the extent to which mesoscale activity can be simulated using a variable resolution mesh. As such, this section compares two variable resolution simulations, $x5\text{-NA-}15\text{ km}$ and $x5\text{-NA-}7.5\text{ km}$ to the quasi-uniform simulation discussed above. Before conducting this detailed comparison, we start with a survey of the global KE field from each of the three simulations on February 1st of Year 15 as shown in Fig. 8.

The largest differences between the three simulations occur outside the NA where the $x1\text{-}15\text{ km}$, $x5\text{-NA-}15\text{ km}$ and $x5\text{-NA-}7.5\text{ km}$ simulations have resolutions of approximately 15 km, 80 km and 40 km, respectively. At 40 km, the $x5\text{-NA-}7.5\text{ km}$ simulation produces Agulhas Rings and weak eddying in the ACC and North Pacific. At 80 km, the $x5\text{-NA-}15\text{ km}$ simulation produces no Agulhas Rings and significantly less eddy activity in the ACC and North Pacific as compared to the other two simulations. Within the NA, the primary difference is that the $x5\text{-NA-}7.5\text{ km}$ is more energetic than the two simulations with 15 km in the NA. The positive impact of increased resolution is also seen in Table 2; finer grid resolution generally implies more accurate representation of section transports.

We note that the retroflection of the North Brazil Current occurs in the mesh transition zone for the $x5\text{-NA-}15\text{ km}$ and $x5\text{-NA-}7.5\text{ km}$ simulations. As the current passes Cabo de Sao Roque and turns northwest, it enters the mesh transition zone. The current passes almost entirely through the mesh transition zone before retroflecting back to the south and reentering the mesh transition zone. Finally,

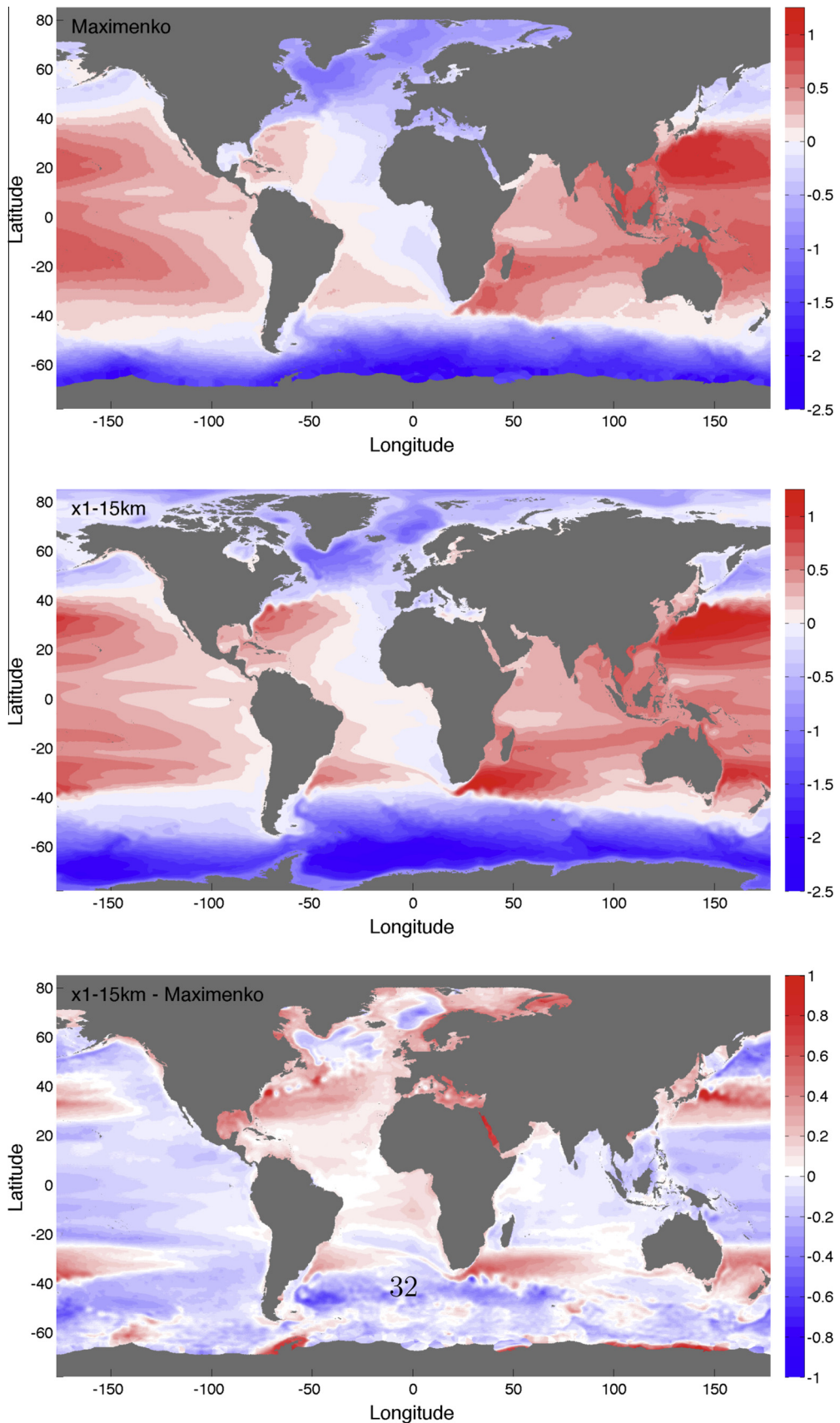


Fig. 6. Mean SSH from observations (top) and from the $x1-15\text{ km}$ simulation (middle). Bottom panel shows $x1-15\text{ km} - \text{observations}$.

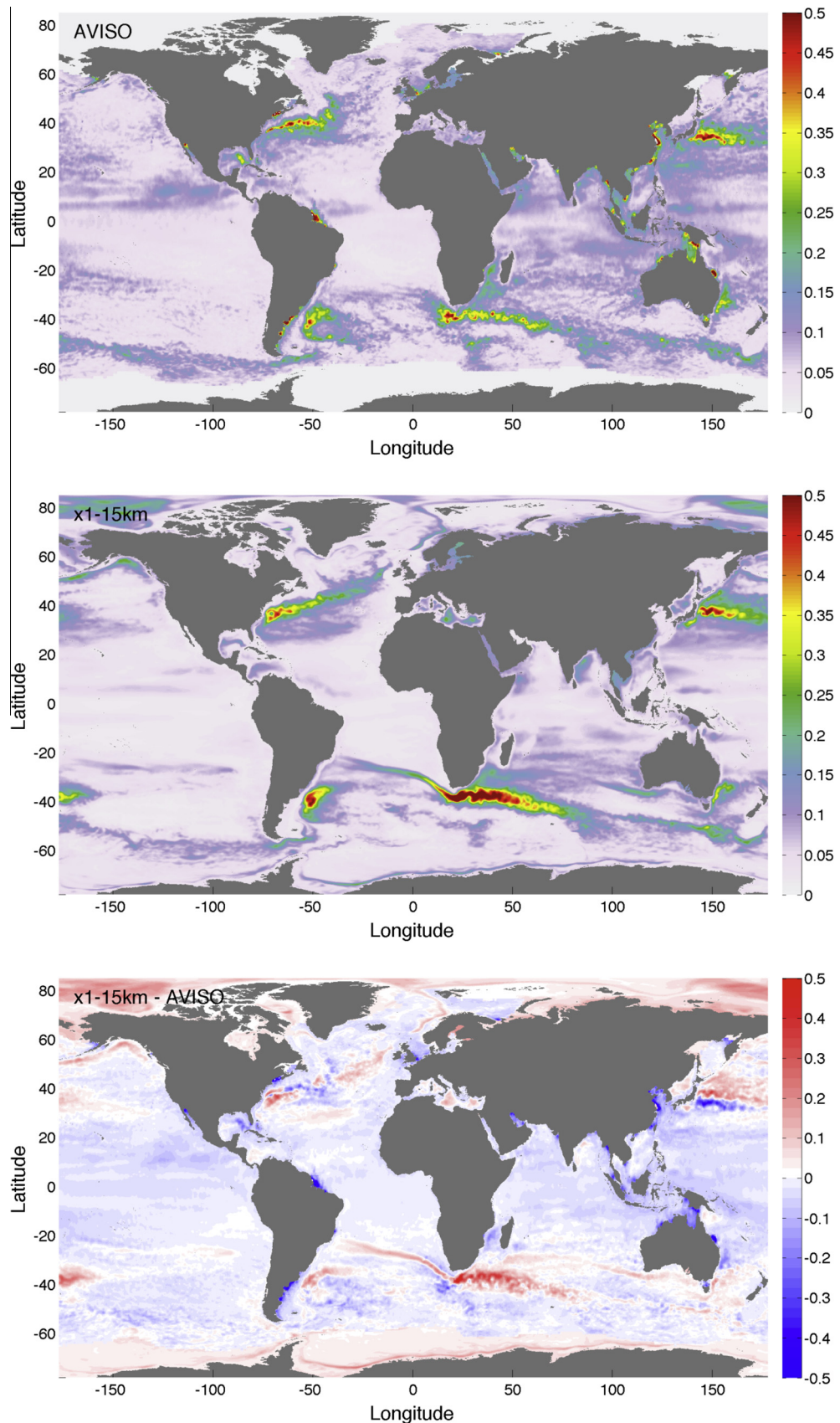


Fig. 7. SSH RMS from observations (top) and from the x1-15 km- simulation (bottom). Bottom panel shows x1-15 km- observations.

Table 2

Transport of major current systems: Simulated time-mean transports (Sv) through common sections are compared to observational estimates. Simulated transports are of the form mean \pm standard-deviation, while observed transports are of the form best-estimate \pm observational-error. Positive values are north and eastward. Observational estimates are from Nowlin and Klinck (1986) (Drake Passage), Ganachaud and Wunsch (2000) (Tasmania-Antarctica), Sprintall et al. (2009) (Indonesian Throughflow) and van der Werf et al. (2010) (Mozambique Channel).

Simulation	Drake	Tasm-Ant	Ind Thru	Agulhas	Mozam
x1-15	148 \pm 3	160 \pm 5	-10.4 \pm 2	-76 \pm 35	-8.6 \pm 4
x5-NA-15	168 \pm 6	179 \pm 8	-8.6 \pm 3	-70 \pm 13	-5.5 \pm 3
x5-NA-7.5	161 \pm 5	172 \pm 7	-9.5 \pm 3	-75 \pm 18	-5.8 \pm 4
obs estimate	134 \pm 14	157 \pm 10	-15 \pm 4	-70 \pm 20	-16 \pm 13

the current exits the mesh transition zone as it moves east to form the Atlantic equatorial undercurrent. So not only is the mesh transition zone “invisible” in Fig. 8, but the transition zone does not inhibit the dynamics of retroflexion in any obvious manner.

The mean SSH anomalies from all three simulations and observations are shown in Fig. 9. Before discussing the patterns in detail, we note that the three simulations are much more similar to each other than to the observations; biases that exist in any one simulation are, for the most part, found in the other simulations. Therefore, discussion of biases relative to observations are meant to pertain to all three simulations, except where noted.

The simulations produce a subtropical gyre with a SSH amplitudes too large by 0.40 m that extends too far into the Atlantic basin. The delayed separation of the Gulf Stream is evident by the poleward extension of the subtropical gyre along the coast. After separation, the simulated mean path of the Gulf Stream tracks the observations very closely.

The SSH amplitudes of the subpolar gyre are too large by approximately 0.25 m. While the overall shape of the subpolar gyre in the simulations compares well with observations, the simulations accentuate the division of the gyre caused by the Reykjanes Ridge. The extension of the observed subpolar gyre as it wraps around the Grand Banks and produces negative SSH anomalies off the southern boundary of Newfoundland is not reproduced in any of the simulations, but the x5-NA-7.5 km does produce slightly more negative SSH anomalies in this region than the other two simulations.

The SSH RMS from all three simulations and observations are shown in Fig. 10. Similar to the mean SSH results, the three simulations are much more similar to each other than to the observations. In the simulations, the Gulf Stream extends along the coast past Cape Hatteras and does not move away from the shelf until reaching Delaware Bay. After separation, the simulated Gulf Stream typically undergoes retroflexion that periodically produces closed, cyclonic eddies that move southwest within the Gulf Stream recirculation gyre. This explains the “donut” in SSH variability located directly east of the Chesapeake Bay; the upper half of the donut is the result of eddies propagating along the Gulf Stream, while the lower half of the donut is the result of cyclonic eddies propagating southwest.

In both the simulations with 15 km resolution in the NA, the axis of maximum variability is rotated about 10° in the counter clockwise direction relative to observations. The simulation with 7.5 km resolution does noticeably better in reproducing the east-west orientation of maximum mesoscale activity. All of the simulations show a Northwest Corner, with the x5-NA-7.5 km being somewhat more accurate than the 15 km simulations. The relatively weak Northwest Corner is overshadowed by the anomalous mesoscale activity in the NA Current south of the Reykjanes Ridge.

All of the simulations produce Gulf of Mexico Loop Rings. The SSH RMS associated with the creation of these loop rings is approximately 50% of the amplitude as observed, with the x5-NA-7.5 km

simulation somewhat closer to observations than the two 15 km simulations.

The simulated transport through various sections within the Caribbean is shown in Table 3. The format is the same as in Table 2; simulated transports are listed as mean with standard deviation and observed transports are listed as best estimate along with observational error. The result from Table 3 is that all simulations produce transports of the correct sign (i.e. the transports are in the right direction) but with an amplitude of approximately 50% of the observed estimate. The other broad result is that resolution seems to improve the simulation as compared to observations; all transports produced by the x5-NA-7.5 km simulation are closer to observations than the two simulations using 15 km resolution.

5.3. Computational performance

Since we have yet to optimize the computational efficiency of MPAS-O, we do not expect the computational performance to be on par with existing IPCC-class models. Yet, we need to provide some evidence that the MPAS-O model could obtain the computational efficiency of models like POP, because it is only the combination of simulation quality and computational efficiency that will produce a compelling alternative to structured-grid models.

Although a more thorough exploration of this model's computational performance is left for a later time, a basic study has been performed to ensure that the model is computationally viable. This initial study was performed on Lobo, a cluster housed at Los Alamos National Laboratory. Lobo contains 4352 AMD Opteron model 8354 cores, each with 2 GB of RAM. Performance of MPAS-O is compared with POP on Lobo for a set of quasi-uniform meshes.

The comparison is made by comparing “stripped-down” versions of MPAS-O and POP. The computational performance is measured using only the simplest numerics: centered-in-space horizontal and advection, explicit vertical mixing and no other physical parameterizations. Furthermore, both models use the same time step. The use of such simple numerics is to ensure that the work per degree of freedom is commensurate between the two models.

Table 4 shows computational performance as measured in Simulated Years Per Day (SYPD) per CPU wall clock day. Larger table entries mean more SYPD for a given number of processors. Computational performance is measured by configuring POP at the common 1° and 0.1° resolutions and by configuring MPAS-O at 60 km, 30 km and 15 km resolutions. Data obtained from POP is scaled to the MPAS-O resolutions and vice versa. The bottom column in Table 4 measures the ratio of POP to MPAS-O performance. These numbers indicate that a stripped-down MPAS-O is slower than a stripped-down POP by a factor of 1.9 to 3.4 at equivalent resolution.

The performance values in Table 4 were obtained by testing each configuration with processor counts ranging from 16 to 1024, and using the best case. Low-resolution configurations are fastest on smaller processor counts, and high-resolution fastest on high processor counts, as one would expect to provide each processor with an appropriate workload. These tests showed good strong scaling over a range of processor counts. For example, using the 30 km grid, throughput in SYPD per CPU wall clock day for processor counts by powers of two from 16 to 1024 were all within 20% of the fastest case (in this metric constant throughput indicates perfect scaling).

Since MPAS-O uses an unstructured grid in the horizontal, neighboring cells, edges and vertices are addressed indirectly. Yet in the vertical, MPAS-O uses structured data addressing, just like all other IPCC-class ocean models. We have exploited the data uniformity in the vertical by defining all arrays with the vertical levels

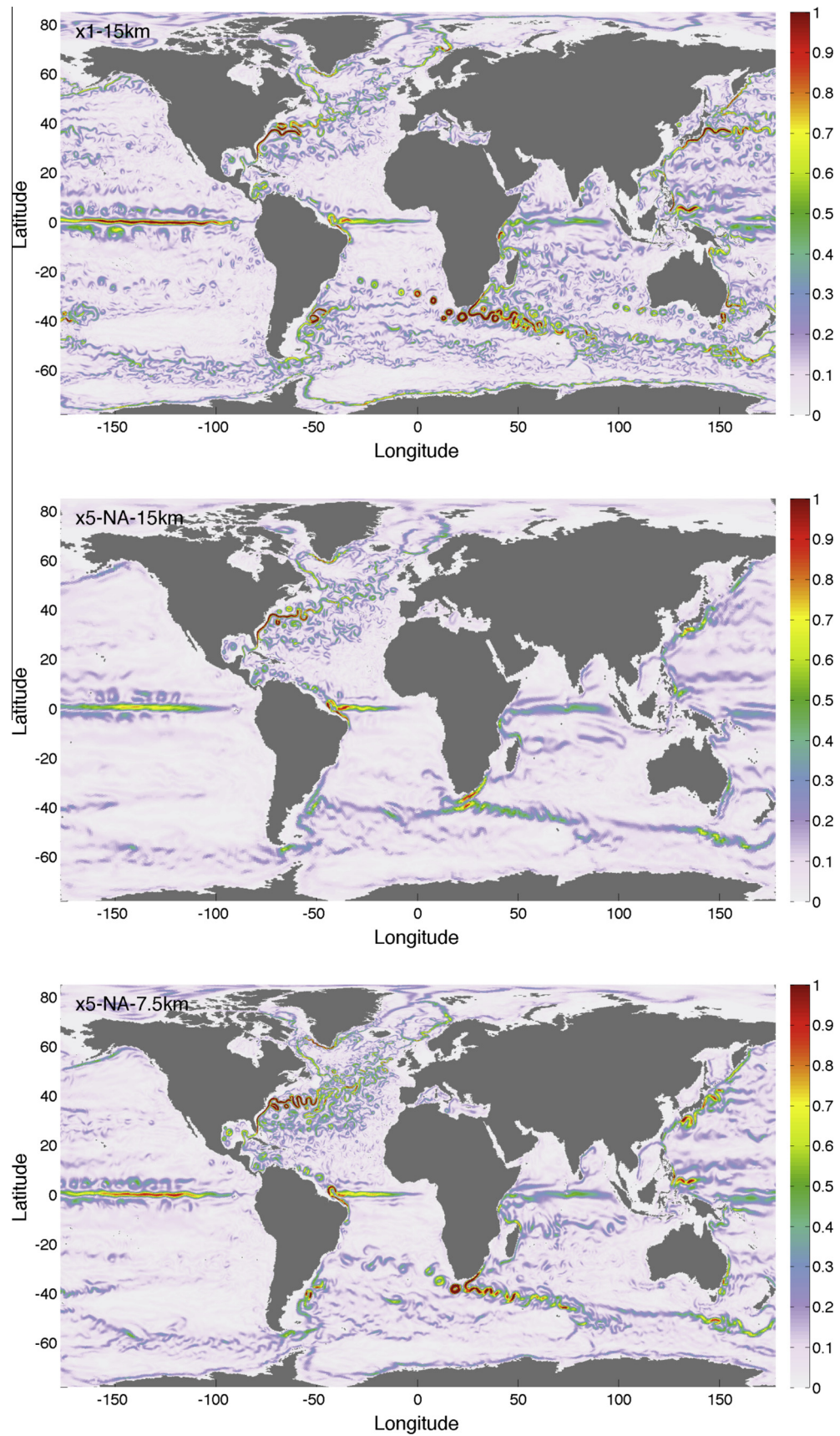


Fig. 8. A snapshot of velocity magnitude from February 1st of Year 15 for the (top) $x1$ -15 km simulation, (middle) $x5$ -NA-15 km and (bottom) $x5$ -NA-7.5 km simulations.

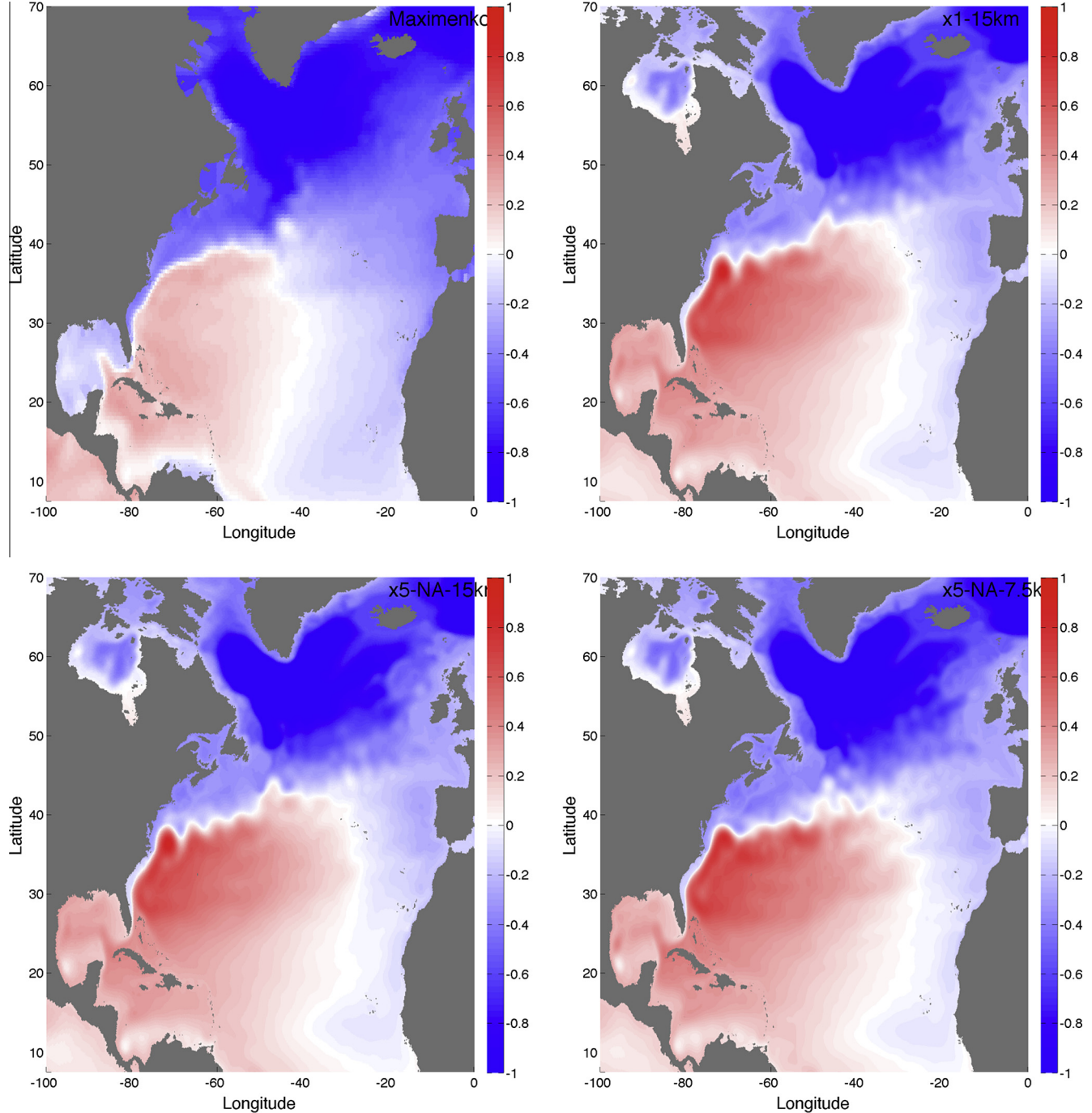


Fig. 9. Mean SSH in the NA from observations (Maximenko), $x1$ -15 km, $x5$ -NA-7.5 km and $x5$ -NA-15 km, moving clockwise from upper left.

as the leading index, thus leading to uniform memory access patterns when looping over the vertical index within Fortran. We speculate that the penalty caused by MPAS-O's indirect addressing in the horizontal is partially averted due to the direct addressing in the vertical. Furthermore, the study by MacDonald et al. (2011) suggests that the penalty for non-uniform data access in the horizontal can be entirely mitigated when there is sufficient computational work per Degree of Freedom (DOF). Using such simple numerics in the stripped-down MPAS-O/POP comparison shown in Table 4 results in very little work per degree-of-freedom, and this tilts the scale against MPAS-O. As we add physical parameterizations, such as KPP (Large et al., 1994) and GM (Gent and McWilliams, 1990), and use higher order numerical methods, we expect that the MPAS-O performance will approach that of POP.

An alternative to the stripped-down comparison is to compare the models in their respective standard configuration at eddy-permitting resolution. In this case, the actual throughput, including I/O, for the $x1$ -15 km simulation is two SYPD on 3000 Lobo processors, which is identical to high resolution simulations of the POP ocean model in its standard high-resolution 0.1° configuration on the same machine (see, e.g. Maltrud et al., 2009).

The above comparisons assume that the value of each DoF in MPAS-O and POP is equal. Thus, a potential pitfall of a comparison based on DoF is that it neglects the “value” of each DoF. In the end,

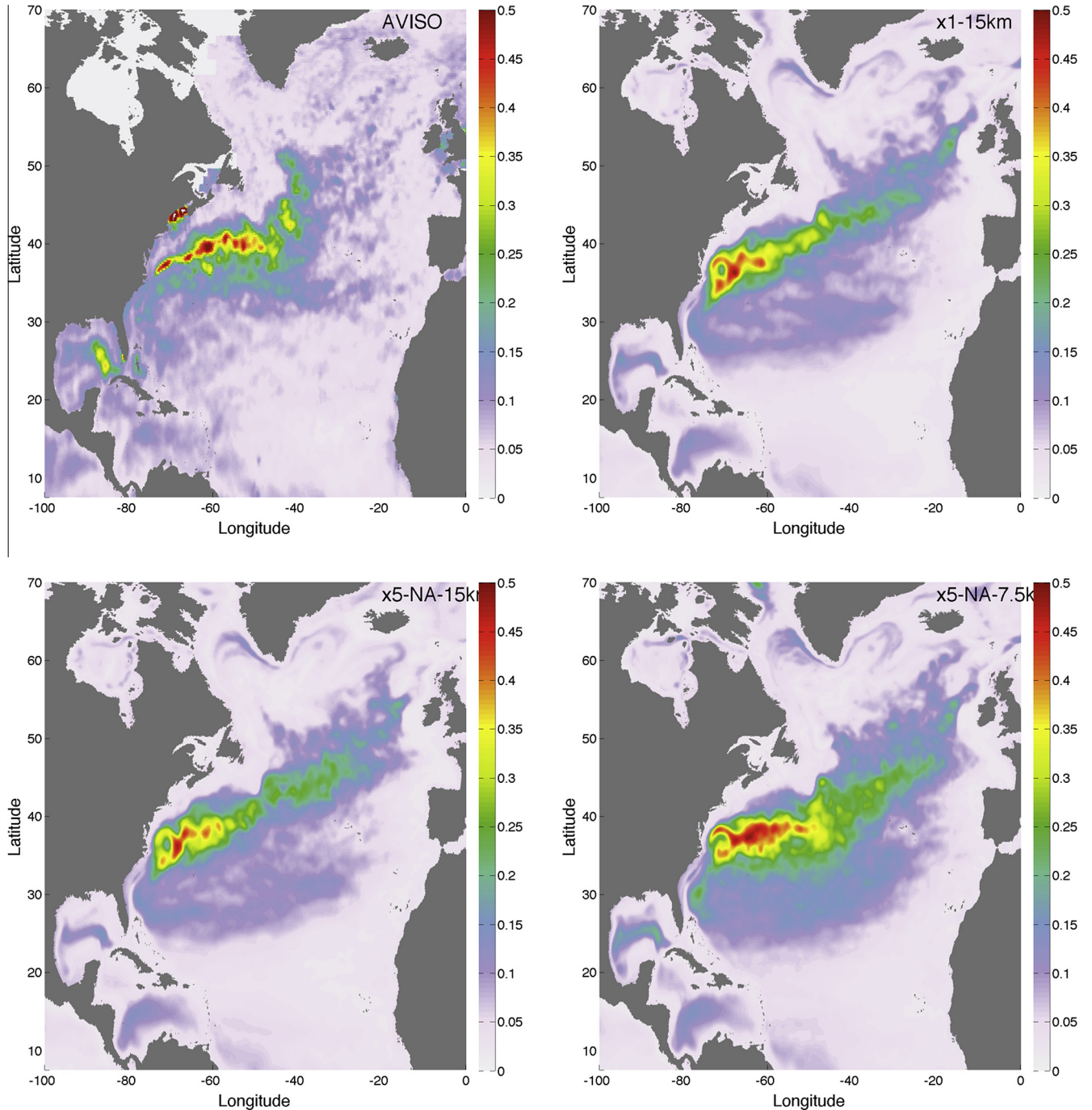


Fig. 10. SSH RMS in the NA from observations (AVISO), $x1\text{-}15\text{ km}$, $x1\text{-}NA\text{-}7.5\text{ km}$ and $x1\text{-}NA\text{-}15\text{ km}$, moving clockwise from upper left.

Table 3

Transports within the Caribbean Region: Simulated time-mean transports through common sections are compared to observational estimates. Simulated transports are of the form mean \pm standard-deviation, while observed transports are of the form best-estimate \pm observational-error. Positive values are northward and eastward. Observational estimates are from Johns et al. (2002) and Roemmich (1981).

Simulation	Antilles	Mona Pass	Wind Pass	FL-Cuba	FL-Baham
$x1\text{-}15\text{ km}$	-7.1 ± 1.8	-1.8 ± 0.6	-4.6 ± 1.8	14.1 ± 1.8	16.5 ± 2.3
$x5\text{-}NA\text{-}15\text{ km}$	-8.7 ± 2.2	-1.9 ± 0.6	-3.9 ± 2.0	14.4 ± 1.7	17.6 ± 2.1
$x5\text{-}NA\text{-}7.5\text{ km}$	-10.3 ± 2.6	-2.1 ± 1.0	-4.8 ± 2.4	17.1 ± 1.5	22.4 ± 2.3
obs estimate	-18.4 ± 4.7	-2.6 ± 1.2	-7.0	31 ± 1.5	31.5 ± 1.5

Table 4

A comparison of computational performance of stripped-down versions of MPAS-O and POP dynamical cores. Each column shows performance at a different resolution. Performance is measured in SYPD per CPU wall clock day, so larger numbers indicate better performance. Resolution increases to the right. Performance data for POP is obtained at 1.0° and 0.1° resolutions and interpolated to the MPAS-O 60, 30 and 15 km resolutions. Performance data for MPAS-O is obtained at 60, 30, and 15 km resolutions and interpolated to the POP 1.0° and 0.1° resolutions. The bottom row shows the ratio of POP to MPAS-O performance.

	1.0°	60 km	30 km	15 km	0.1°
MPAS-O	1.5×10^{-1}	5.5×10^{-2}	7.0×10^{-3}	8.0×10^{-4}	2.6×10^{-4}
POP	2.8×10^{-1}	1.1×10^{-1}	1.9×10^{-2}	2.5×10^{-3}	9.0×10^{-4}
Ratio	1.9	2.0	2.7	3.2	3.4

we wish to measure the quality of the simulation per computational cost, which is a more difficult and nuanced metric to obtain. We are currently attempting to measure “quality per cost” for MPAS-O and POP using an idealized, mesoscale eddy resolving, ocean test case.

6. Discussion and conclusions

The numerical method recently developed by Thuburn et al. (2009) and Ringler et al. (2010) is extended to solve the 3D, hydrostatic, Boussinesq equations for the simulation of the global ocean circulation. The novel aspect of this model is its ability to accurately simulate geophysical flows on a mesh that contains a wide range of grid scales. In particular, the model employs a host of other numerical methods that can be considered to be “state-of-the-art”, such as an Arbitrary-Lagrangian–Eulerian vertical coordinate, a monotone tracer transport scheme and a split-explicit time-stepping algorithm.

The motivation for the MPAS modeling framework is primarily due to the fact that the approach allows access to multi-resolution meshes, while providing an underlying finite-volume, numerical method that is robust on time scales commensurate with climate modeling. Furthermore, it accomplished this with acceptable computational efficiency. As described in Section 2, the approach allows for the creation of multi-resolution meshes based on a single scalar function, the mesh-density function, that is both intuitive and flexible. The guarantee of mesh quality (Gersho, 1979) means that one does not have to become an expert in mesh-generation technology to generate high-quality grids. In this contribution we have deployed the SCVT mesh generation tool in a very conservative manner; the meshes have a single high-resolution region in the NA that is only 5× the resolution of the low-resolution grid. Based on the results in Ringler et al. (2011), ocean simulations that employ meshes with 20× or more in grid variation seem readily attainable. In addition, more physics-based approaches to mesh generation, such as enhanced resolution in coastal regions or in the vicinity of narrow sills and channels are waiting to be explored.

In terms of validating this modeling approach, we posed two questions. The first question to be addressed was as follows: does the global, quasi-uniform simulation ($x1\text{-}15\text{ km}$) do a fair job at reproducing the observed structure of the major current systems, ocean gyres and mesoscale activity? While the $x1\text{-}15\text{ km}$ certainly has biases that we will elaborate on below, the simulation qualitatively and, often, quantitatively reproduces the observational data. First, the transports of the major current systems shown in Table 2 are surprisingly similar to the observational estimates. We find the results surprising because absolutely no tuning was done to improve these currents. With the exceptions discussed below, the magnitude and location of mesoscale eddy activity is well represented in the $x1\text{-}15\text{ km}$ simulation.

In terms of biases, the simulated SSH amplitudes of the subtropical and subpolar gyres shown in Fig. 6 are too large by 0.25 to 0.40 m as compared to observations (Maximenko et al., 2009). The Agulhas Rings are too strong and long-lived, resulting in too much SSH variance in the South Atlantic. The $x1\text{-}15\text{ km}$ simulation supports a frontal boundary on the equatorward side of New Zealand resulting in a region of mesoscale eddy activity that has no analog in the observational data set. Also, while a weak Northwest Corner is present in the $x1\text{-}15\text{ km}$ simulation, the NA Current extends to the northeast with too much eddy activity in the vicinity of Reykjanes Ridge.

The transports through important sections (see Table 2) are within observational error for the $x1\text{-}15\text{ km}$ simulation. Within the Caribbean Region (see Table 3), the simulated transports of the $x1\text{-}15\text{ km}$ simulation are too weak by about 50%. In simulations on the timescale of the thermohaline circulation, we might expect

the value of these transports to change. The transport values shown in Tables 2 and 3 should be regarded as provisional until confirmed by multi-decadal simulations.

Many of the biases described above are typical for ocean models at eddying resolution. For example, overshooting in the separation of eastern boundary currents has been a problem for over two decades e.g., Semtner et al. (1992), Maltrud et al. (1998) and Maltrud and McClean (2005). Significant improvements to the separation of the Gulf Stream and the structure of the Northwest Corner were seen in the 0.1° POP simulation of Maltrud et al. (2009) compared to Maltrud and McClean (2005), likely due to the inclusion of partial bottom cells (Adcroft et al., 1997). We expect similar improvements in the near future when partial bottom cells are implemented in this model.

We can also attribute some of the model's deficiencies to the approximations made in forcing these ocean-only simulations. First, the biases in SSH are very similar to those found in McClean et al. (2011) when forcing POP with the same normal-year CORE wind stress data. In our simulations and in McClean et al. (2011) the subtropical and subpolar gyres are too strong. In addition, SST and SSS are restored to WOCE monthly-mean data with a restoring time scale of 30 days. We expect that the results will improve significantly by computing surface stress, heat and freshwater fluxes through bulk formulae based on 6-hourly atmosphere and ocean state variables. We will follow up on this below.

The second question addressed was as follows: can the representation of the NA produced by the $x1\text{-}15\text{ km}$ simulation be reproduced by the $x5\text{-NA-15 km}$ simulation? The answer to this question is unequivocally “yes”. In terms of mean SSH in the NA (Fig. 9), SSH RMS in the NA (Fig. 10) and transports throughout the Caribbean (Table 3), the $x1\text{-}15\text{ km}$ and $x5\text{-NA-15 km}$ are essentially identical. It is important to note that the “perfect” $x5\text{-NA-15 km}$ simulation would be an exact reproduction of both the positive and negative aspects of the $x1\text{-}15\text{ km}$ simulation within the NA region.

The $x5\text{-NA-7.5 km}$ simulation uses approximately the same computing resources as the $x1\text{-}15\text{ km}$ simulation, but redistributes grid points in order to obtain higher resolution in the NA at the expense of resolution elsewhere. In terms of simulating the NA, this redistribution of grid points appears to be beneficial. Relative to the 15 km simulations, the transports throughout the Caribbean are markedly improved and the SSH RMS is better represented. Whether or not this reallocation of computer resources is beneficial will depend entirely on the questions being asked of the model simulation. At this point we simply note that as opposed to traditional, structured-grid global ocean models, such a reallocation is easily accomplished with this modeling approach.

As mentioned above, our hypothesis is that some of the major deficiencies found in the simulations can be removed by forcing the model in a more realistic manner. To test this hypothesis we are currently coupling MPAS-O into the NCAR/DOE Community Earth System Model. The atmosphere counterpart to MPAS-O is already coupled into the CESM (Rauscher et al., 2013). Given the vetting that this numerical method has undergone during the development and evaluation of the four dynamical cores referenced in the Introduction, we have reason to be confident in the method's ability to simulate the global ocean system. Furthermore, the model still lacks advanced physical parameterizations such as KPP (Large et al., 1994) and a mesoscale eddy parameterization of any type, either seminal (Gent and McWilliams, 1990) or prospective (Ringler and Gent, 2011). Thus, our approach is two-pronged. Based on the results presented above, the first research track is to continue to increase the realism of MPAS-O by including advanced parameterizations and including more realistic forcing. On the second research track we will develop a robust test-suite following Ilicak et al. (2012) to carefully quantify the fidelity of the underlying numerical approach in ocean-specific configurations.

While our stated focus of this contribution was the characterization of the dynamical core, we could not entirely omit the need for scale-adaptive parameterizations. While we omit a mesoscale eddy parameterization in these simulations, we are still obligated to provide a horizontal turbulence closure that dissipates the downscale cascade of energy and/or enstrophy. The use of constant viscosity or constant biharmonic viscosity is not only untenable, but impractical; the constant coefficient is either insufficient to control noise in the low resolution regions or overly dissipative in the high-resolution regions. Left with few alternatives, we included in the model a biharmonic viscosity that scales as dx^3 and the Leith turbulence closure that also scales as dx^3 . While such choices can be supported by the literature and from theory, we have no reason to believe that our choices are anything more than simply acceptable. Having anticipated that the lack of scale-adaptive parameterizations will limit the utility of this new modeling approach, we have begun to systematically evaluate closures for mesoscale large-eddy simulations (Pietarila Graham and Ringler, 2013) and to explore new extensions to old closures (Ringler and Gent, 2011).

The current performance results shown in Table 4 lead us to believe that while MPAS-O is not as efficient as other ocean models, the computational performance is sufficient to continue forward with the intention of producing an IPCC-class global ocean model. In addition, performance tests have shown that the MPAS-O code scales well to thousands of processors at high resolution. Actual throughput, including I/O, for the $x1\text{-}15\text{ km}$ simulation is two SYPD on 3000 processors, which is identical to high resolution simulations of the POP ocean model in its standard high-resolution 0.1° configuration on the same machine (see, e.g. Maltrud et al., 2009). We expect that the computational performance of MPAS-O will improve substantially as we begin to exploit accelerated architectures that are currently becoming available.

The model presented above demonstrates the ability to solve the 3D primitive equations on a mesh that contains multiple grid scales with acceptable computational performance. Beyond the novelty of solving the equations with variable grid sizes, the method is a typical finite volume approach. Finite volume approaches are exceptionally well suited to modeling the global ocean on climate-change time scales. As such, we view this model as a strong candidate for successfully modeling the global ocean circulation on time scales of centuries to millennia. But the reality is that solving a system of partial differential equations on a mesh with multiple scales is the easy part. The hard part, in our view, is developing the full suite of parameterizations that work sensibly, i.e. without *ad hoc* tuning, across a wide range of truncation scales. The end goal is to pair this multi-resolution partial differential equation solver with a suite of scale-adaptive physical parameterizations to produce a truly multi-scale simulation of the global ocean system.

Acknowledgements

This ocean model is being developed as a part of the MPAS project to produce a shared software framework for the development of dynamical cores. This work would not have been possible without the contributions from the broad MPAS development team and, in particular, the contributions of Michael Duda. The manuscript benefited from the comments of Sergey Danilov and two anonymous reviewers. The altimeter products were produced by Ssalto/Duacs and distributed by Aviso, with support from Cnes (<http://www.aviso.oceanobs.com/duacs/>). The authors thank Gregory Johnson for providing observational data of the Equatorial Undercurrent. Simulations were conducted using LANL Institutional Computing resources. This work was supported by the Earth System Modeling and Regional and Global Climate Modeling programs of the Office of Biological and Environmental Research within the US Department of Energy's Office of Science.

Appendix A. MPAS-Ocean equations of motion

A.1. Continuous equations

We assume that the fluid fills a three-dimensional domain, Ω . We decompose the boundary, $\partial\Omega$, into the portion of the fluid in contact with the solid wall, $\partial\Omega^w$, and the moving free-surface of the fluid, $\partial\Omega^s$, that can be uniquely identified by its z-coordinate, $z^s(x, y)$. Within Ω we wish to solve the following set of equations:

$$\nabla_3 \cdot \mathbf{v} = 0, \quad (\text{A.1})$$

$$\frac{\partial \mathbf{u}}{\partial t} + \eta \mathbf{k} \times \mathbf{u} + w \frac{\partial \mathbf{u}}{\partial z} = -\frac{1}{\rho_0} \nabla p - \nabla K + \mathbf{D}_h^u + \mathbf{D}_v^u \quad (\text{A.2})$$

$$\frac{\partial \tilde{\rho} \varphi}{\partial t} + \nabla \cdot (\tilde{\rho} \varphi \mathbf{u}) + \frac{\partial}{\partial z} (\tilde{\rho} \varphi w) = D_h^\varphi + D_v^\varphi, \quad (\text{A.3})$$

$$p(x, y, z) = p^s(x, y) + \int_z^{z^s} \rho g dz' \quad (\text{A.4})$$

$$\rho = f_{eos}(\Theta, S, p). \quad (\text{A.5})$$

Eqs. A.1 through A.5 are a normal expression of the primitive equations; i.e. the incompressible Boussinesq equations in hydrostatic balance. The exact form of the pseudo-density, $\tilde{\rho}$, will be specified below in A.25. Variable definitions are in Tables A.1 and A.2. Note that \mathbf{v} is the three-dimensional velocity, \mathbf{u} is the horizontal velocity, and w the vertical velocity, i.e. $\mathbf{v} = \mathbf{u} + w\mathbf{k}$. The momentum advection and Coriolis terms in (A.2) are presented in vorticity-kinetic energy form (Ringler et al., 2010, Eq. 5). MPAS-Ocean includes several choices for the equation of state (A.5); Jackett and McDougall, 1995 was used for the simulations presented.

Table A.1

Latin variables used in prognostic equation set. Column 3 shows the native horizontal grid location. All variables are located at the center of the layer in the vertical.

Symbol	Name	Grid	Notes
$\mathbf{D}_h^u, \mathbf{D}_v^u$	mom. diffusion terms	edge	h horizontal, v vertical
D_h^φ, D_v^φ	tracer diff. terms	cell	
f	Coriolis parameter	vertex	
f_{eos}	equation of state	—	
F	thickness flux	edge	$F = hu$
g	grav. acceleration	constant	
G	barotropic mom.	edge	
	forcing		
h	layer thickness	cell	
H	total unperturbed depth	cell	
\mathbf{k}	vertical unit vector		
K	kinetic energy	edge	$K = \mathbf{u} ^2/2$
p	pressure	cell	
p^s	surface pressure	cell	
q	potential vorticity	vertex	$q = \eta/h$
S	salinity	cell	a tracer φ
S	model state	—	
t	time	—	
T^u, T^h, T^φ	tendencies	—	
u	horizontal velocity	edge	normal component to edge
\mathbf{u}	horizontal velocity	—	
\mathbf{v}	3D velocity	—	
w	vertical transport	cell	determined by coord. type
z	vertical coordinate	—	positive upward
z^{mid}	layer mid-depth location	cell	

Table A.2

Greek variables used in prognostic equation set. Column 3 shows the native horizontal grid location. All variables are located at the center of the layer in the vertical.

Symbol	Name	Grid	Notes
δ	horizontal divergence	cell	$\delta = \nabla \cdot \mathbf{u}$
ζ	sea surface height	cell	
η	absolute vorticity	vertex	$\eta = \mathbf{k} \cdot \nabla \times \mathbf{u} + f$
Θ	potential temperature	cell	a tracer φ
κ_h, κ_v	diffusion	cell	
v_h, v_v	viscosity	edge	
ρ	density	cell	
ρ_0	reference density	constant	
φ	tracer	cell	e.g. Θ, S

The diffusion terms are left unspecified because there are several choices available within the model. The standard vertical diffusion is

$$\mathbf{D}_v^u = \frac{\partial}{\partial z} \left(v_v \frac{\partial \mathbf{u}}{\partial z} \right), \quad (\text{A.6})$$

$$D_v^\varphi = \tilde{\rho} \frac{\partial}{\partial z} \left(\kappa_v \frac{\partial \varphi}{\partial z} \right), \quad (\text{A.7})$$

where the vertical viscosity v_v and diffusion κ_v may be computed with a variety of vertical mixing schemes. In the simulations presented in this paper, horizontal tracer diffusion is zero and horizontal momentum diffusion uses a biharmonic operator and the Leith closure, as described in Section 3.5. For the purpose of illustrating the discretization methods in this appendix, we use a simple Laplacian operator,

$$\mathbf{D}_h^u = v_h \nabla^2 \mathbf{u} = v_h (\nabla \delta + \mathbf{k} \times \nabla \eta), \quad (\text{A.8})$$

$$D_h^\varphi = \nabla \cdot (\tilde{\rho} \kappa_h \nabla \varphi). \quad (\text{A.9})$$

The form of \mathbf{D}_h^u used in (A.8) only conserves solid-body rotation when v_h is constant. The pseudo-density, $\tilde{\rho}$, in (A.7) and (A.9) will be replaced with the thickness h in the next section. The momentum diffusion is in divergence-vorticity form because it is a natural discretization of the vector Laplacian operator with a C-grid staggering.

A.2. Derivation of thickness and tracer equation

The continuous form of the continuity equation when using an Arbitrary-Lagrangian-Eulerian vertical coordinate is not frequently derived. We show it here for completeness and to serve as a foundation for the remainder of the model description in this appendix. Consider an arbitrary control volume $V(t)$ that may evolve in time, enclosed by the surface ∂V that is moving with velocity \mathbf{v}_r (Fig. A.1a). Stated within the context of the Reynold's Transport Theorem (Kundu et al., 2012, p. 88) conservation of mass is expressed as

$$\frac{d}{dt} \int_{V(t)} \varphi dV + \int_{\partial V(t)} \varphi (\mathbf{v} - \mathbf{v}_r) \cdot \mathbf{n} dA = 0 \quad (\text{A.10})$$

where $\mathbf{v}(x, y, z, t)$ is the Eulerian velocity and \mathbf{n} is a unit vector normal to the surface at the differential surface area dA . The variable $\varphi(x, y, z, t)$ may be the fluid density ρ or the density-weighted concentration of some tracer, in units of tracer mass per volume.

Before deriving the ocean model thickness equation, it is useful to look at the limits of (A.10). If $V(t)$ is a true Lagrangian control volume, then the velocity of the boundary surface ∂V is identical to \mathbf{v} , i.e. $\mathbf{v}_r = \mathbf{v}$. Thus,

$$\frac{d}{dt} \int_{V(t)} \varphi dV = 0 \quad (\text{A.11})$$

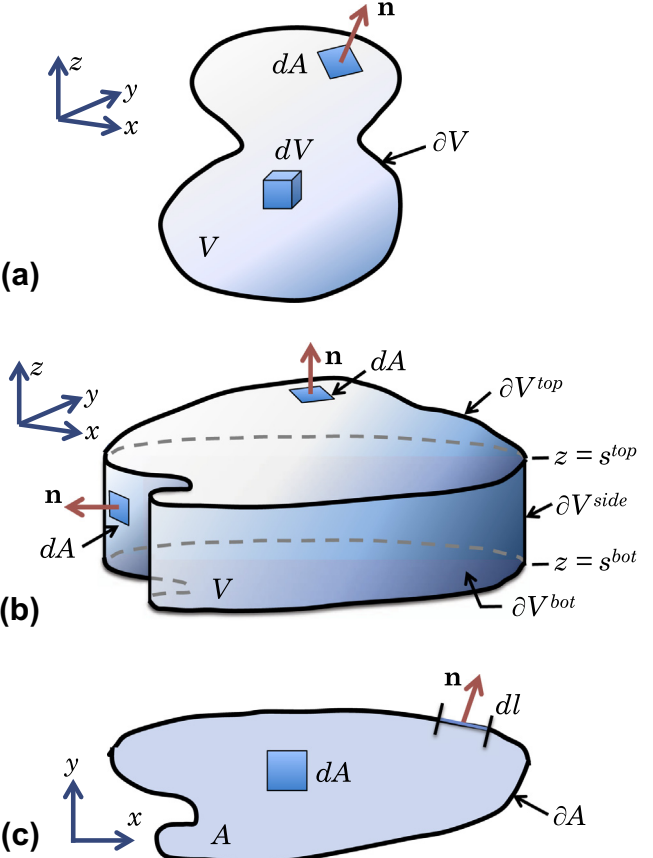


Fig. A.1. Control volume for Reynold's Transport Theorem (a), after restricting the control volume to fixed horizontal boundaries (b), and a two-dimensional horizontal cross-section of the control volume (c).

where $V_L(t)$ denotes a Lagrangian control volume. Eq. (A.11) is the statement of conservation of mass in the Lagrangian reference frame (see Eq. (3) of Ringler, 2011). If, instead, $V(t)$ is fixed, then \mathbf{v}_r is zero and

$$\frac{d}{dt} \int_{V_E} \varphi dV + \int_{\partial V_E} \varphi \mathbf{v} \cdot \mathbf{n} dA = 0 \quad (\text{A.12})$$

which is a common Eulerian expression for conservation of mass (see Eq. (17) of Ringler (2011)).

Next, we assume that the control volume V is bounded in the horizontal by a fixed wall ∂V^{side} that does not vary in time or z (Fig. A.1b). The top and bottom boundaries of V , ∂V^{top} and ∂V^{bot} , occur at $z = s^{\text{top}}(x, y, t)$ and $z = s^{\text{bot}}(x, y, t)$, respectively, where $s^{\text{top}} > s^{\text{bot}}$ for all x, y and t . Conservation of mass for this control volume is

$$\begin{aligned} \frac{d}{dt} \int_{V(t)} \varphi dV + \int_{\partial V^{\text{side}}} \varphi (\mathbf{v} - \mathbf{v}_r) \cdot \mathbf{n} dA + \int_{\partial V^{\text{top}}(t)} \varphi (\mathbf{v} - \mathbf{v}_r) \cdot \mathbf{n} dA \\ + \int_{\partial V^{\text{bot}}(t)} \varphi (\mathbf{v} - \mathbf{v}_r) \cdot \mathbf{n} dA = 0. \end{aligned} \quad (\text{A.13})$$

To highlight the different treatment of the horizontal and vertical directions, recall that $\mathbf{v} = \mathbf{u} + w\mathbf{k}$, where \mathbf{u} is the horizontal velocity, so that $\mathbf{u} \cdot (w\mathbf{k}) = 0$. On the fixed side boundary ∂V^{side} the normal vector is horizontal and boundary velocity is zero, so $(\mathbf{v} - \mathbf{v}_r) \cdot \mathbf{n} = \mathbf{u} \cdot \mathbf{n}$. To simplify, only consider the vertical velocities through the top and bottom surfaces, so that $\mathbf{v} \cdot \mathbf{n} = \mathbf{v} \cdot \mathbf{k} = w$ along ∂V^{top} and $\mathbf{v} \cdot \mathbf{n} = \mathbf{v} \cdot (-\mathbf{k}) = -w$ along ∂V^{bot} . In other words, we are ignoring any horizontal components of $\mathbf{v} \cdot \mathbf{n}$ that occur due to a tilted top or bottom surface. Then

$$\begin{aligned} \frac{d}{dt} \int_{V(t)} \varphi dV + \int_{\partial V^{\text{side}}} \varphi \mathbf{u} \cdot \mathbf{n} dA + \int_{\partial V^{\text{top}}(t)} \varphi (w - w_r) dA \\ - \int_{\partial V^{\text{bot}}(t)} \varphi (w - w_r) dA = 0. \end{aligned} \quad (\text{A.14})$$

Next, we rewrite the conservation equation with two-dimensional horizontal integrals over A , the horizontal cross-section of V . The boundary of A is ∂A and dl is a differential length along ∂A (Fig. A.1c).

$$\begin{aligned} \frac{d}{dt} \int_A \int_{s^{\text{bot}}}^{s^{\text{top}}} \varphi dz dA + \int_{\partial A} \left(\int_{s^{\text{bot}}}^{s^{\text{top}}} \varphi \mathbf{u} dz \right) \cdot \mathbf{n} dl + \int_A [\varphi (w - w_r)]_{z=s^{\text{top}}} dA \\ - \int_A [\varphi (w - w_r)]_{z=s^{\text{bot}}} dA = 0. \end{aligned} \quad (\text{A.15})$$

For the last two terms we have made the assumption that the area of the top and bottom surface is the same as A . Define the thickness as

$$h(x, y, t) = s^{\text{top}}(x, y, t) - s^{\text{bot}}(x, y, t) \quad (\text{A.16})$$

and the vertical average of a variable within the control volume as

$$\bar{\phi}^z(x, y, t) = \frac{1}{h} \int_{s^{\text{bot}}}^{s^{\text{top}}} \phi(x, y, z, t) dz \quad (\text{A.17})$$

so that the conservation equation becomes

$$\begin{aligned} \frac{d}{dt} \int_A h \bar{\phi}^z dA + \int_{\partial A} h \bar{\phi}^z \mathbf{u} \cdot \mathbf{n} dl + \int_A [\varphi w_{\text{tr}}]_{z=s^{\text{top}}} dA \\ - \int_A [\varphi w_{\text{tr}}]_{z=s^{\text{bot}}} dA = 0, \end{aligned} \quad (\text{A.18})$$

where $w_{\text{tr}} = w - w_r$ is the transport through the top and bottom surfaces.

We now average all the variables over the area A and take the limit as the area is reduced to a point, i.e., the control volume is reduced to a vertical line, so that the variables are discretized into layers in the vertical but are continuous in the horizontal. Define the averaging operators

$$\tilde{A} = \int_A dA \quad (\text{A.19})$$

$$\bar{\phi}^A(t) = \frac{1}{\tilde{A}} \int_A \phi(x, y, t) dA \quad (\text{A.20})$$

so that (A.18) becomes

$$\frac{d}{dt} h \bar{\phi}^A + \frac{1}{\tilde{A}} \int_{\partial A} h \bar{\phi}^z \mathbf{u} \cdot \mathbf{n} dl + \overline{[\varphi w_{\text{tr}}]_{z=s^{\text{top}}}}^A - \overline{[\varphi w_{\text{tr}}]_{z=s^{\text{bot}}}}^A = 0. \quad (\text{A.21})$$

Note that A is the set of points of the cross-section, while \tilde{A} is a scalar value of the area of A . Taking the limit as the cross-sectional area \tilde{A} goes to zero,

$$\lim_{A \rightarrow (x, y)} \bar{\phi}^A = \phi(x, y). \quad (\text{A.22})$$

The definition of the weak form of the divergence is given as

$$\nabla \cdot \mathbf{F} = \lim_{A \rightarrow (x, y)} \frac{\int_{\partial A} \mathbf{F} \cdot \mathbf{n} dl}{\int_A dA}. \quad (\text{A.23})$$

Applying the limit to (A.21),

$$\frac{\partial}{\partial t} h \bar{\phi}^z + \nabla \cdot (h \bar{\phi}^z \mathbf{u}) + \varphi w_{\text{tr}}|_{z=s^{\text{top}}} - \varphi w_{\text{tr}}|_{z=s^{\text{bot}}} = 0. \quad (\text{A.24})$$

This is a conservation equation for a fluid constituent of thickness-weighted concentration φ in a two-dimensional horizontal layer with thickness h . For the mass of the fluid itself, φ is simply the fluid density. For a Boussinesq fluid, perturbations in density

are assumed to be small and the remaining constant density may be divided out, so that the continuity equation for the pseudo-density, $\bar{\rho}$, is

$$\frac{\partial h}{\partial t} + \nabla \cdot (h \bar{\mathbf{u}}^z) + w_{\text{tr}}|_{z=s^{\text{top}}} - w_{\text{tr}}|_{z=s^{\text{bot}}} = 0. \quad (\text{A.25})$$

This is often called the thickness equation.

If we assume that $w_r = w$ at every point in the fluid, i.e. that our control volumes are Lagrangian control volumes, then the transport across any layer is $w_{\text{tr}} = 0$ and we have

$$\frac{\partial h}{\partial t} + \nabla \cdot (h \bar{\mathbf{u}}^z) = 0 \quad (\text{A.26})$$

which is the isopycnal expression of conservation of volume. If, instead, we assume that $s^{\text{top}} = z_1$ and $s^{\text{bot}} = z_2$, i.e. assume z-level surfaces such that h is no longer a function of x, y or t , then $w_r = 0$ and $w_{\text{tr}} = w$. In addition, let $(s^{\text{top}} - s^{\text{bot}}) \rightarrow 0$ to obtain

$$\nabla \cdot \mathbf{u} + \frac{\partial w}{\partial z} = 0. \quad (\text{A.27})$$

This is the strong form of conservation of volume written in an Eulerian reference frame.

A.3. Vertical discretization

We now discretize the equations of motion in the vertical, indexed by k , where $z = 0$ is the mean elevation of the free surface, the z coordinate is positive upward, $k = 1$ is the top layer, and k increases downward. The discrete vertical operators on a generic variable ϕ are defined as

$$(\bar{\phi}^t)_k^m = (\phi_k^t + \phi_{k+1}^t)/2 \quad (\text{A.28})$$

$$(\bar{\phi}^m)_k^t = (\phi_{k-1}^m + \phi_k^m)/2 \quad (\text{A.29})$$

$$\delta z_k^m(\phi^t) = \frac{\phi_k^t - \phi_{k+1}^t}{h_k} \quad (\text{A.30})$$

$$\delta z_k^t(\phi^m) = \frac{\phi_{k-1}^m - \phi_k^m}{(\bar{h})_k^t} \quad (\text{A.31})$$

where the superscripts m and t denote the location as the middle or top of cell k in the vertical. Colons in subscripts are a placeholder for the vertical index, and indicate that multiple layers are used by the vertical operator. In this section variables remain continuous in the horizontal and in time, and $\phi_k^m(x, y, t)$ is the vertical average of ϕ in the layer k , written as $\bar{\phi}^z$ in the previous section for the control volume. All variables except h and w represent a vertical average over the layer, and the m superscript is omitted for simplicity. The thickness h is just a single value for the layer. The variable w_k^t is henceforth defined to be the transport of fluid across the top interface of layer k , i.e. redefined to be w_{tr} as used in the previous section. The model equations with vertical discretization are

$$\begin{aligned} \frac{\partial u_k}{\partial t} + q_k h_k u_k^\perp + \overline{[w_k^t \delta z^t(u)]}_k^m \\ = -\frac{1}{\rho_0} \nabla p_k - \frac{\rho_k g}{\rho_0} \nabla z_k^{\text{mid}} - \nabla K_k + v_h (\nabla \delta_k + \mathbf{k} \times \nabla \eta_k) \\ + \delta z_k^m(v_\nu \delta z^t(u)) \end{aligned} \quad (\text{A.32})$$

$$\frac{\partial h_k}{\partial t} + \nabla \cdot (h_k \mathbf{u}_k) + w_k^t - w_{k+1}^t = 0, \quad (\text{A.33})$$

$$\begin{aligned} \frac{\partial(h_k \varphi_k)}{\partial t} + \nabla \cdot (h_k \mathbf{u}_k \varphi_k) + \bar{\varphi}_k^t w_k^t - \bar{\varphi}_{k+1}^t w_{k+1}^t \\ = \nabla \cdot (h_k \kappa_h \nabla \varphi_k) + h_k \delta z_k^m(\kappa_\nu \delta z^t(\varphi)) \end{aligned} \quad (\text{A.34})$$

Variable definitions are in Tables A.1 and A.2. Horizontal gradients are within each layer, rather than along constant z -surfaces. This coordinate transformation results in the addition of the z^{mid} gradient term in the momentum equation. This term compensates for pressure gradients in sloping layers that should not cause spurious motion, and is derived in (Adcroft and Campin, 2004, Section A.2).

The arguments inside the vertical operators receive indices to replace the colon once the operator is applied. For example,

$$\begin{aligned} \overline{[w^t \delta z^t(u.)]}_k^m &= \frac{1}{2} (w_k^t \delta z_k^t(u.) + w_{k+1}^t \delta z_{k+1}^t(u.)) \\ &= \frac{1}{2} \left(w_k^t \frac{u_{k-1} - u_k}{(h)_k^t} + w_{k+1}^t \frac{u_k - u_{k+1}}{(h)_{k+1}^t} \right) \end{aligned} \quad (\text{A.35})$$

The Arbitrary Lagrangian–Eulerian (ALE) coordinate offers a great deal of freedom to choose among vertical grid types. ALE is implemented in the computation of the vertical transport through the layer interface, w^t . For idealized isopycnal vertical coordinates, w^t is simply set to zero, so there is no vertical transport of thickness, tracers, or momentum. For z -level, w^t is computed from (A.33) with $\partial h / \partial t = 0$ for $k > 1$ so that layer thicknesses remain constant. In z -star coordinates, w^t is computed so that sea surface height (SSH) perturbations are distributed throughout the column. When using idealized isopycnal coordinates, the ∇p and ∇z^{mid} terms in (A.32) may be replaced with the gradient of a Montgomery potential (Higdon, 2005 Eq. 1).

A.4. Horizontal discretization

The horizontal grids are based on Spherical Centroidal Voronoi Tessellations, and are described in detail in Section 2. The discrete horizontal operators on a generic vector field \mathbf{F} and generic scalar field ϕ are

$$[\nabla \cdot \mathbf{F}]_i = \frac{1}{A_i} \sum_{e \in EC(i)} n_{e,i} F_e l_e, \quad (\text{A.36})$$

$$[\nabla \phi]_e = \frac{1}{d_e} \sum_{i \in CE(e)} -n_{e,i} \phi_i, \quad (\text{A.37})$$

$$[\mathbf{k} \cdot (\nabla \times \mathbf{F})]_v = \frac{1}{A_v} \sum_{e \in EV(v)} t_{e,v} F_e d_e, \quad (\text{A.38})$$

where subscripts i, e , and v index the discretized variables through cell centers, edges, and vertices, respectively (Fig. 3). In this C-grid formulation, scalar values ϕ_i are located at cell centers and the discretized vector field F_e is the normal component at an edge. Thus the divergence is applied to edges and results in a cell-centered quantity; the gradient moves from cell centers to edges; and the vorticity from edges to vertices. Here A_i is the cell area, d_e is the distance between cell centers, l_e is edge length, A_v is the area of the dual cell around v , $n_{e,i}$ indicates the sign of the vector at edge e with respect to cell i , and $t_{e,v}$ keeps track of whether a positive F_e makes a positive or negative contribution to the curl function at the vertex v . The sets $EC(i)$ are the edges about cell i ; $CE(e)$ are the cells neighboring edge e ; and $EV(v)$ are the edges radiating from vertex v . Detailed explanations and figures may be found in Section 3 of Ringler et al. (2010).

The model equations with horizontal discretization are

$$\begin{aligned} \frac{\partial u_{k,e}}{\partial t} + \widehat{q}_{k,e} F_{k,e}^\perp + \overline{[\widehat{w}_{:,e}^t \delta z^t(u_{:,e})]}_k^m \\ = -\frac{1}{\rho_0} [\nabla p_{k,:}]_e - \frac{\widehat{\rho}_{k,e} g}{\rho_0} [\nabla z_{k,:}^{mid}]_e - [\nabla K_{k,:}]_e \\ + v_h ([\nabla \delta_{k,:}]_e + [\mathbf{k} \times \nabla \widehat{\eta}_{k,:}]_e) + \delta z_k^m (v_v \delta z^t(u_{:,e})) \end{aligned} \quad (\text{A.39})$$

$$\frac{\partial h_{k,i}}{\partial t} + [\nabla \cdot \mathbf{F}_{k,:}]_i + w_{k,i}^t - w_{k+1,i}^t = 0, \quad (\text{A.40})$$

$$\begin{aligned} \frac{\partial(h_{k,i}\varphi_{k,i})}{\partial t} + [\nabla \cdot (\mathbf{F}_{k,:} \widehat{\varphi}_{k,:})]_i + \overline{\varphi}_{k,i}^t w_{k,i}^t - \overline{\varphi}_{k+1,i}^t w_{k+1,i}^t \\ = [\nabla \cdot (\widehat{h}_{k,:} \kappa_h \nabla \varphi_{k,:})]_i + h_{k,i} \delta z_k^m (\kappa_v \delta z^t(\varphi_{:,i})). \end{aligned} \quad (\text{A.41})$$

$$p_{k,i} = p_i^s + \sum_{k'=1}^{k-1} \rho_{k',i} g h_{k',i} + \frac{1}{2} \rho_{k,i} g h_{k,i} \quad (\text{A.42})$$

$$\rho_{k,i} = f_{eos}(\Theta_{k,i}, S_{k,i}, p_{k,i}). \quad (\text{A.43})$$

Variable definitions are in Tables A.1 and A.2. The first subscripted index is the vertical layer, and the second is the horizontal index. Colons in subscripts indicate that multiple vertical layers were used for a vertical operator (first index), or that multiple edges or cell centers are used in computing the horizontal operator (second index). Here $F_{k,e} = \widehat{h}_{k,e} u_{k,e}$ is the thickness flux and $F_{k,e}^\perp$ is the thickness flux in the direction perpendicular to F_e . The C-grid discretization only contains the normal component of vectors at each edge (Fig. 3). The prognostic velocity $u_{k,e}$, flux $F_{k,e}$, and all gradients are normal to edge e . The tangential velocity $u_{k,e}^\perp$, as well as meridional and zonal velocities at cell centers, are computed diagnostically using averaging operators. The variables $u_{k,e}$ and $F_{k,e}^\perp$ are not bold in (A.39) because they are the normal and tangential components, respectively, of full vectors.

The $(\widehat{\cdot})_e$ and $(\widehat{\cdot})_v$ symbols represent the averaging of a variable from its native location to an edge or vertex. The potential vorticity is most naturally located at vertices and is computed as

$$q_{k,v} = \eta_{k,v} / \widehat{h}_{k,v} = ([\mathbf{k} \cdot \nabla \times u_{k,:}]_v + f_v) / \widehat{h}_{k,v}. \quad (\text{A.44})$$

The boundary conditions for (A.39–A.41) are impermeable and no-slip. The sides and bottom are impervious to flow, so that $u_{k,e} = 0$ on all boundary edges, and $w_{k,i}^t = 0$ at the bottom surface. The vertical transport through the sea surface is zero, i.e. $w_{1,:}^t = 0$. Inflow and outflow boundary conditions may be set up for specific domains. The no-slip boundary condition is implemented via the computation of the relative vorticity, $[\mathbf{k} \cdot \nabla \times u_{k,:}]_v$, at those vertices that reside along the boundary. The relative vorticity at vertices along the boundary is computed assuming that the tangential velocity at the wall is zero. If desired, one may use a free-slip boundary condition by setting $[\mathbf{k} \cdot \nabla \times u_{k,:}]_v = 0$ at vertices along the boundary. This is equivalent to assuming that the velocity tangent to the boundary has no gradient normal to the boundary.

A.5. Temporal discretization

For convenience we rewrite (A.39–A.41) as

$$\frac{\partial u_{k,e}}{\partial t} = T_{k,e}^u(\mathcal{S}), \quad (\text{A.45})$$

$$\frac{\partial h_{k,i}}{\partial t} = T_{k,i}^h(\mathcal{S}), \quad (\text{A.46})$$

$$\frac{\partial(h_{k,i}\varphi_{k,i})}{\partial t} = T_{k,i}^\varphi(\mathcal{S}), \quad (\text{A.47})$$

where T variables are the tendency terms and \mathcal{S} is the model state, i.e. all variables used in computing the tendencies. The model equations now fit into standard notation for time-stepping routines.

Due to the time step restrictions discussed in Section 3.3, a split-explicit time-stepping method is used in the simulations presented in this paper. Define the barotropic and baroclinic velocities as

$$\bar{u}_e = \sum_k \hat{h}_{k,e} u_{k,e} / \sum_k \hat{h}_{k,e} \quad (\text{A.48})$$

$$u'_{k,e} = u_{k,e} - \bar{u}_e, \quad (\text{A.49})$$

$$\zeta_i = \sum_k h_{k,i} - H_i \quad (\text{A.50})$$

Here ζ is the sea surface height perturbation and H_i is the total unperturbed column depth. The barotropic momentum and thickness equations are

$$\frac{\partial \bar{u}_e}{\partial t} = -f \bar{u}_e^\perp - g[\nabla \zeta]_e + G_e, \quad (\text{A.51})$$

$$\frac{\partial \zeta_i}{\partial t} + \left[\nabla \cdot \left(\bar{u}_e \sum_k \hat{h}_{k,:} \right) \right]_i = 0, \quad (\text{A.52})$$

where G includes all remaining terms in the barotropic equation (Higdon, 2005, Eq. 5). The Coriolis and pressure gradient terms remain outside the G term because these are the first-order terms involved in surface gravity waves that require the short barotropic time step. Subtracting the barotropic Eq. (A.51) from the total momentum Eq. (A.39), one obtains the baroclinic momentum equation,

$$\frac{\partial u'_{k,e}}{\partial t} = T'_{k,e}(S) - f u'_{k,e}^\perp + g[\nabla \zeta]_e - G_e, \quad (\text{A.53})$$

where $T'_{k,e} = T_{k,e}^u + f u_{k,e}^\perp$, i.e. the Coriolis force is explicitly written rather than remaining in T^u .

The split explicit time-stepping method is summarized as follows.

- Initialize by computing \bar{u}_e^n , $u_{k,e}^n$, and ζ_i^n using (A.48–A.50)
- **Stage 1: Baroclinic velocity (3D)**

$$\tilde{u}_{k,e}^{n+1} = u_{k,e}^n + \Delta t \left(-f u_{k,e}^{n,\perp} + T'_{k,e}(S^n) + g[\nabla \zeta]_e \right) \quad (\text{A.54})$$

$$G_e = \frac{1}{\Delta t} \sum_k \hat{h}_{k,e} \tilde{u}_{k,e}^{n+1} / \sum_k \hat{h}_{k,e} \quad (\text{A.55})$$

$$u_{k,e}^{n+1} = \tilde{u}_{k,e}^{n+1} - \Delta t G_e \quad (\text{A.56})$$

- **Stage 2: Barotropic velocity (2D)**

◊ Advance \bar{u} and ζ as a coupled system through $j = 0 : 2J - 1$ subcycles, ending at time $t^n + 2\Delta t$.

$$\bar{u}_e^{n+(j+1)/J} = \bar{u}_e^{n+j/J} + \frac{\Delta t}{J} \left(-f \bar{u}_e^{n+j/J\perp} - g[\nabla \zeta]_e^{n+j/J} + G_e \right) \quad (\text{A.57})$$

$$\zeta_i^{n+(j+1)/J} = \zeta_i^{n+j/J} - \frac{\Delta t}{J} \left[\nabla \cdot \left(\bar{u}_e^{n+j/J} \left(\zeta_i^{n+j/J} + \hat{H}_e \right) \right) \right]_i \quad (\text{A.58})$$

◊ Average subcycles in time.

$$(\bar{u}_{avg})_e^{n+1} = \frac{1}{2J+1} \sum_{j=0}^{2J} \bar{u}_e^{n+j/J} \quad (\text{A.59})$$

- **Stage 3: Update thickness, tracers, density and pressure**

◊ ALE step: compute $(w^t)_i^{n+1}$.
 ◊ Compute T^h , T^φ using velocities, averaged in time, from Stages 1 and 2.

$$h_{k,i}^{n+1} = h_{k,i}^n + \Delta t T_{k,i}^h \quad (\text{A.60})$$

$$\varphi_{k,i}^{n+1} = \frac{1}{h_{k,i}^{n+1}} \left[h_{k,i}^n \varphi_{k,i}^n + \Delta t T_{k,i}^\varphi \right] \quad (\text{A.61})$$

- ◊ compute $\rho_{i,k}^{n+1}$, $p_{i,k}^{n+1}$, $(v_v)_{e,k}^{n+1}$, $(\kappa_v)_{i,k}^{n+1}$
- ◊ Revise $u_{k,e}^{n+1}$, $\varphi_{k,i}^{n+1}$ with implicit vertical mixing.

This algorithm summary has been greatly simplified for brevity. Stage 1 and each subcycle of Stage 2 may be iterated to update velocity and SSH variables, and a weighted average between new and old may be specified for each variable. The full algorithm is repeated in a predictor–corrector process. Thus what is written as a forward Euler step in this write-up is a backwards Euler or Crank–Nicolson step on the second iteration. These iterations improve the stability of the split explicit algorithm, allowing for larger overall time-steps and fewer barotropic subcycles. While the present time-stepping algorithm worked well for the high resolution simulations presented here, future work will determine the best combination of iterations and weighting for stability and efficiency.

A small barotropic correction is added to the velocities used to compute the tendencies in Stage 3 to ensure that the vertical sum of total thickness fluxes through each cell edge matches the barotropic flux. This, along with the fact that the tracer equation (A.60) reduces to the thickness equation (A.61) for a constant tracer, guarantees tracer conservation to machine precision.

References

- Adcroft, A., Campin, J., 2004. Rescaled height coordinates for accurate representation of free-surface flows in ocean circulation models. *Ocean Modelling* 7 (3–4), 269–284.
- Adcroft, A., Hill, C., Marshall, J., 1997. Representation of topography by shaved cells in a height coordinate ocean model. *Monthly Weather Review* 125 (9), 2293–2315.
- Bleck, R., 2002. An oceanic general circulation model framed in hybrid isopycnic–Cartesian coordinates. *Ocean Modelling* 4 (1), 55–88.
- Bryan, K., 1969. A numerical method for the study of the circulation of the world ocean. *Journal of Computational Physics* 4 (3), 347–376.
- Chen, C., Liu, H., Beardsley, R., 2003. An unstructured grid, finite-volume, three-dimensional, primitive equations ocean model: application to coastal ocean and estuaries. *Journal of Atmospheric and Oceanic Technology* 20 (1), 159–186.
- Cox, M., 1970. A mathematical model of the Indian Ocean. *Deep Sea Research and Oceanographic Abstracts* 17 (1), 47–75.
- Danilov, S., Kivman, G., Schröter, J., 2004. A finite-element ocean model: principles and evaluation. *Ocean Modelling* 6 (2), 125–150.
- Du, Q., Gunzburger, M., 1999. Centroidal Voronoi tessellations: applications and algorithms. *SIAM Review* 41 (4), 637–676.
- Fang, F., Morrow, R., 2003. Evolution, movement and decay of warm-core Leeuwin Current eddies. *Deep Sea Research Part II: Topical Studies in Oceanography* 50 (12–13), 2245–2261.
- Fox-Kemper, B., Menemenlis, D., 2008. Can large eddy simulation techniques improve mesoscale-rich ocean models? Eddy resolving ocean models. *Geophysical Monograph* 177, 319–338.
- Ganachaud, A., Wunsch, C., 2000. Improved estimates of global ocean circulation, heat transport and mixing from hydrographic data. *Nature* 408, 453–457.
- Gent, P., McWilliams, J., 1990. Isopycnal mixing in ocean circulation models. *Journal of Physical Oceanography* 20 (1), 150–155.
- Gersho, A., 1979. Asymptotically optimal block quantization. *IEEE Transactions on Information Theory* 25 (4), 373–380.
- Gouretski, V., Koltermann, K.P., 2004. WOCE global hydrographic climatology. *Berichte des BSH* 35, 1–52.
- Griffies, S.M., Adcroft, A., Banks, H., Boning, C.W., Chassignet, E.P., Danabasoglu, G., Danilov, S., Deleersnijder, E., Drange, H., England, M., 2009. Problems and prospects in large-scale ocean circulation models. In: Hall, J., Harrison, D.E., Stammer, D. (Eds.), *Proceedings of the OceanObs’09 Conference: Sustained Ocean Observations and Information for Society*, ESA Publication WPP-306 ESA, Venice, pp. 21–25.
- Hallberg, R., 1997. Stable split time stepping schemes for large-scale ocean modeling. *Journal of Computational Physics* 135 (1), 54–65.
- Hecht, M.W., Hunke, E., Maitrud, M.E., Petersen, M.R., Wingate, B.A., 2008. Lateral mixing in the eddying regime and a new broad-ranging formulation. Eddy resolving ocean models. *Geophysical Monograph* 177, 339–352.
- Higdon, R., 2005. A two-level time-stepping method for layered ocean circulation models: further development and testing. *Journal of Computational Physics* 206 (2), 463–504.
- Ilicak, M., Adcroft, A., Griffies, S.M., Hallberg, R., 2012. Spurious dianeutral mixing and the role of momentum closure. *Ocean Modelling* 45–46, 37–58.
- Jackett, D.R., McDougall, T.J., 1995. Minimal adjustment of hydrographic profiles to achieve static stability. *Journal of Atmospheric and Oceanic Technology* 12 (2), 381–389.
- Jacobsen, D.W., Gunzburger, M., Ringler, T., Burkhardt, J., Peterson, J., 2013. Parallel algorithms for planar and spherical Delaunay construction with an application

- to centroidal Voronoi tessellations. *Geoscientific Model Development Discussions* 6, 1427–1466.
- Johns, W., Townsend, T., Frantoni, D., Wilson, W., 2002. On the Atlantic inflow to the Caribbean Sea. *Deep Sea Research Part I: Oceanographic Research* 49, 211–243.
- Johnson, G.C., Sloyan, B.M., Kessler, W.S., McTaggart, K.E., 2002. Direct measurements of upper ocean currents and water properties across the tropical Pacific during the 1990s. *Progress in Oceanography* 52 (1), 31–61.
- Ju, L., Du, Q., Gunzburger, M., 2002. Probabilistic methods for centroidal Voronoi tessellations and their parallel implementations. *Parallel Computing* 28 (10), 1477–1500.
- Ju, L., Ringler, T., Gunzburger, M., 2010. Voronoi tessellations and their application to climate and global modeling. Numerical techniques for global atmospheric models. In: Lauritzen, P.H., Jablonowski, C., Taylor, M.A., Nair, R.D. (Eds.), Springer Lecture Notes in Computational Science and Engineering, pp. 1–30.
- Kundu, P.K., Cohen, I.M., Dowling, D.R., 2012. *Fluid Mechanics*, fifth ed. Academic Press.
- Large, W.G., McWilliams, J.C., Doney, S.C., 1994. Oceanic vertical mixing: a review and a model with a nonlocal boundary layer parameterization. *Reviews of Geophysics* 32 (4), 363–403.
- Large, W.G., Pond, S., 1982. Sensible and latent heat flux measurements over the ocean. *Journal of Physical Oceanography* 12, 464–482.
- Large, W.G., Yeager, S., 2004. Diurnal to Decadal Global Forcing for Ocean and Sea-ice Models: The Data Sets and Flux Climatologies.
- Leclair, M., Madec, G., 2011. z-Coordinate, an Arbitrary Lagrangian–Eulerian coordinate separating high and low frequency motions. *Ocean Modelling* 37 (3), 139–152.
- Legeckis, R., 1977. Long waves in the eastern equatorial Pacific Ocean: a view from a geostationary satellite. *Science* 197 (4309), 1179–1181.
- Leith, C., 1996. Stochastic models of chaotic systems. *Physica D: Nonlinear Phenomena* 98 (2–4), 481–491.
- Lloyd, S., 1982. Least squares quantization in PCM. *IEEE Transactions on Information Theory* 28, 129–137.
- MacDonald, A.E., Middlecoff, J., Henderson, T., Lee, J.L., 2011. A general method for modeling on irregular grids. *International Journal of High Performance Computing Applications* 25 (4), 392–403.
- Maltrud, M., Bryan, F., Peacock, S., 2009. Boundary impulse response functions in a century-long eddying global ocean simulation. *International Journal of Computer & Information Sciences* 10 (1–2), 275–295.
- Maltrud, M., McClean, J., 2005. An eddy resolving global 1/10 ocean simulation. *Ocean Modelling* 8 (1–2), 31–54.
- Maltrud, M.E., Smith, R., Semtner, A.J., Malone, R.C., 1998. Global eddy-resolving ocean simulations driven by 1985–1995 atmospheric winds. *Journal of Geophysical Research* 103 (C13), 30825–30853.
- Maximenko, N., Niiler, P., Centurioni, L., Rio, M.-H., Melnichenko, O., Chambers, D., Zlotnicki, V., Galperin, B., 2009. Mean dynamic topography of the ocean derived from satellite and drifting buoy data using three different techniques. *Journal of Atmospheric and Oceanic Technology* 26 (9), 1910–1919.
- McClean, J.L., Bader, D.C., Bryan, F.O., Maltrud, M.E., Mirin, A.A., Jones, P.W., Kim, Y.Y., Ivanova, D.P., Vertenstein, M., 2011. A prototype two-decade fully-coupled fine-resolution CCSM simulation. *Ocean Modelling* 39, 10–30.
- Middleton, J.F., Cirano, M., 2002. A northern boundary current along Australia's southern shelves: the Flinders current. *Journal of Geophysical Research* 107, 3129.
- Murray, R.J., Reason, C., 2001. A curvilinear version of the Bryan–Cox–Semtner Ocean Model and its representation of the Arctic circulation. *Journal of Computational Physics* 171 (1), 1–46.
- Newman, D., 1982. The hexagon theorem. *IEEE Transactions on Information Theory* 28, 137–139.
- Nowlin Jr., W.D., Klinck, J.M., 1986. The physics of the Antarctic circumpolar current. *Journal of Geophysical Research* 24 (3), 469–491.
- Okabe, A., Boots, B., Sugihara, K., Chiu, S., 2009. *Spatial Tessellations: Concepts and Applications of Voronoi Diagrams*. Wiley.
- Pacanowski, R., Philander, S., 1981. Parameterization of vertical mixing in numerical models of tropical oceans. *Journal of Physical Oceanography* 11 (11), 1443–1451.
- Perego, M., Gunzburger, M., Burkardt, J., 2012. Parallel finite-element implementation for higher-order ice-sheet models. *Journal of Glaciology* 58 (207), 76–88.
- Pietarila Graham, J., Ringler, T., 2013. A framework for the evaluation of turbulence closures used in mesoscale ocean large-eddy simulations. *Ocean Modelling* 65, 25–39.
- Randall, D., Bony, S., 2007. Climate Models and Their Evaluation. IPCC WG1 Fourth Assessment Report.
- Rauscher, S.A., Ringler, T.D., Skamarock, W.C., Mirin, A.A., 2013. Exploring a global multiresolution modeling approach using aquaplanet simulations. *Journal of Climate* 26, 2432–2452.
- Renka, R., 1997. Algorithm 772. STRIPACK: Delaunay triangulation and Voronoi diagrams on the surface of a sphere. *ACM Transactions on Mathematical Software* 23, 416–434.
- Ringler, T., 2011. Momentum, vorticity and transport: Considerations in the design of a finite-volume dynamical core. Numerical techniques for global atmospheric models. In: Lauritzen, P.H., Jablonowski, C., Taylor, M.A., Nair, R.D. (Eds.), Springer Lecture Notes in Computational Science and Engineering vol. 80, pp. 143–183.
- Ringler, T., Gent, P., 2011. An eddy closure for potential vorticity. *Ocean Modelling* 39, 125–134.
- Ringler, T., Ju, L., Gunzburger, M., 2008. A multiresolution method for climate system modeling: application of spherical centroidal Voronoi tessellations. *Ocean Dynamics* 58 (5), 475–498.
- Ringler, T., Thuburn, J., Klemp, J., Skamarock, W., 2010. A unified approach to energy conservation and potential vorticity dynamics for arbitrarily-structured C-grids. *Journal of Computational Physics* 229 (9), 3065–3090.
- Ringler, T.D., Jacobsen, D., Gunzburger, M., Ju, L., Duda, M., Skamarock, W., 2011. Exploring a multiresolution modeling approach within the shallow-water equations. *Monthly Weather Review* 139 (11), 3348–3368.
- Roemmich, D., 1981. Circulation of the Caribbean Sea: a well-resolved inverse problem. *Journal of Geophysical Research* 86 (C9), 7993–8005.
- Schouten, M.W., de Ruijter, W.P.M., van Leeuwen, P.J., 2002. Upstream control of Agulhas Ring shedding. *Journal of Geophysical Research* 107 (C8), 3109–3120.
- Semtner Jr., A.J., Chervin, R.M., 1992. Ocean general circulation from a global eddy-resolving model. *Journal of Geophysical Research* 97 (C4), 5493–5550.
- Semtner, A.J., Dec, 1974. An oceanic general circulation model with bottom topography. *Numerical Simulation of Weather and Climate*. Meteorology Department, University of California, Los Angeles.
- Shchepetkin, A.F., McWilliams, J.C., 2005. The regional oceanic modeling system (ROMS): a split-explicit, free-surface, topography-following-coordinate oceanic model. *Ocean Modelling* 9 (4), 347–404.
- Skamarock, W.C., Klemp, J.B., Duda, M.G., Fowler, L.D., Park, S., Ringler, T.D., 2012. A multiscale nonhydrostatic atmospheric model using centroidal Voronoi tessellations and C-grid staggering. *Monthly Weather Review* 140 (9), 3090–3105.
- Skamarock, W., Gassmann, A., 2011. Conservative transport schemes for spherical geodesic grids: high-order flux operators for ODE-based time integration. *Monthly Weather Review* 139 (9), 2962–2975.
- Smagorinsky, J., 1963. General circulation experiments with the primitive equations. *Monthly Weather Review* 91 (3), 99–164.
- Smith, R., Kortas, S., Meltz, B., 1995. Curvilinear coordinates for global ocean models. Los Alamos, preprint LA-UR-95-1146.
- Smith, R., Maltrud, M., Bryan, F., Hecht, M., 2000. Numerical simulation of the North Atlantic Ocean at 1/10. *Journal of Physical Oceanography* 30 (7).
- Sprintall, J., Wijffels, S.E., Molcard, R., Jaya, I., 2009. Direct estimates of the Indonesian Throughflow entering the Indian Ocean: 2004–2006. *Journal of Geophysical Research* 114 (C7), C07001.
- Thuburn, J., Ringler, T., Skamarock, W., Klemp, J., 2009. Numerical representation of geostrophic modes on arbitrarily structured C-grids. *Journal of Computational Physics* 228 (22), 8321–8335.
- van der Werf, P.M., van Leeuwen, P.J., Ridderinkhof, H., de Ruijter, W.P.M., 2010. Comparison between observations and models of the Mozambique Channel transport: seasonal cycle and eddy frequencies. *Journal of Geophysical Research* 115 (C2), C02002.
- White, L., Deleersnijder, E., Legat, V., 2008. A three-dimensional unstructured mesh finite element shallow-water model, with application to the flows around an island and in a wind-driven, elongated basin. *Ocean Modelling* 22 (1), 26–47.
- Williamson, 1992. A standard test set for numerical approximations to the shallow water equations in spherical geometry. *Journal of Computational Physics* 102, 211–224.
- Zalesak, S., 1979. Fully multidimensional flux-corrected transport algorithms for fluids. *Journal of Computational Physics* 31 (3), 335–362.